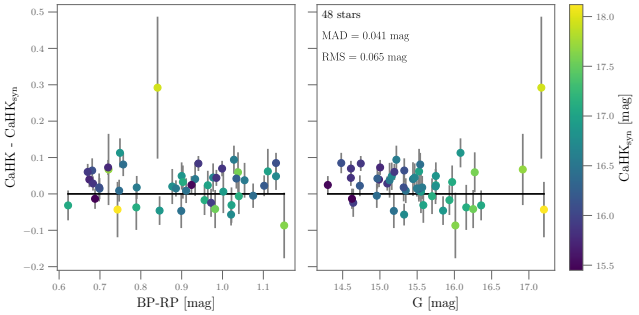

Fig. 32. Residuals of the synthetic photometry of Ca H and K for a sample of 48 stars from Aguado et al. (2019) as a function of $G_{BP}-G_{RP}$ colour and G magnitude, *left* and *right panels*, respectively. These stars have spectroscopic [Fe/H] < -2 dex. The colours of the symbols reflect their CaHK synthetic magnitudes. We highlight the zero deviation line in grey. The residuals do not seem to correlate with $G_{BP}-G_{RP}$ colour.

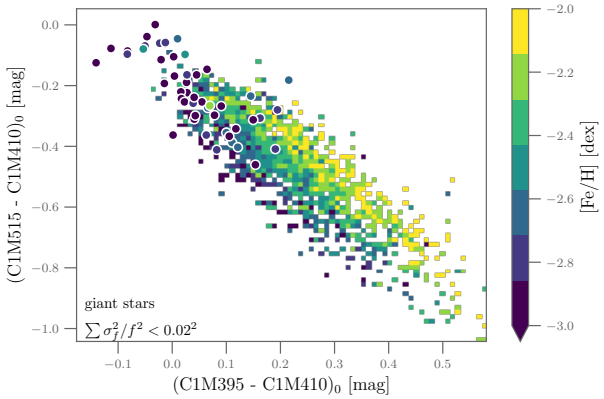

Fig. 33. C1 colour-colour diagram sensitive to metallicity and corrected for extinction. The histogram shows the distribution of a random subset of 5112 giant stars with [Fe/H] < -2 dex from Huang et al. (2022) with a total fractional flux uncertainty in the C1 bands of below 0.02. The colours refer to their photometric iron abundance estimates with the scale on the right-hand size. The round symbols indicate the 48 stars (not only giants) from Pristine discussed in Sect. 5.4 on the same scale using their spectroscopic estimates. The x and y axes are equivalent to CaII and MgH indices, respectively.

half a million very metal-poor stars. Their method to estimate APs exploits multiple colour relations and often depends on distinguishing giants and dwarfs. Of those, we extracted a random sample of about 26 000 giant stars with XP spectra in *Gaia* DR3, which provided us with [Fe/H] and A_0 estimates. We used the *Gaia* EDR3 extinction relations to obtain A_G and further the relations from Appendix H to obtain the coefficients in the C1 bands.

Figure 33 shows in the (C1M396−C1M410) versus (C1M515−C1M410) colours the stars that have a total fractional uncertainty of

$$\frac{\sigma_f}{f} \equiv \sqrt{\left(\frac{\sigma_{C1M395}}{f_{C1M395}}\right)^2 + \left(\frac{\sigma_{C1M410}}{f_{C1M410}}\right)^2 + \left(\frac{\sigma_{C1M515}}{f_{C1M515}}\right)^2} < 0.02. \quad (20)$$

The metallicity gradient is strikingly visible, demonstrating the reliability of the C1-based indices even in the very metal-poor regime.

We remark that (C1M396−C1M410) colour is nearly equivalent to the (CaHK−C1M410) colour. Therefore, we indicated on Fig. 33 the previously mentioned Pristine stars for comparison. The latter are not specifically giant stars, but are mostly turn-off stars, and therefore concentrate in the top left corner of the plot. However, they also agree with the scale from Pristine. This comparison allows us to draw the conclusion that XPSP can transfer knowledge from SkyMapper to Pristine (or the other way around if the latter sample is larger). In particular, this means a common metallicity scale, which is often an issue when comparing surveys. Finally, the XP spectra will offer a significantly large suite of passbands to explore metallicity estimates in a very new manner across the entire sky.

One major limitation of the XPSP is that very metal-poor stars are intrinsically faint in *BP*. As *Gaia* DR3 limits the availability of the stellar XP spectra to $G < 17.65$ mag, a large fraction of the sources in Aguado et al. (2019) and Huang et al. (2022) remain beyond the reach of *Gaia* DR3. However, XPSP data offer a robust set of photometric calibrators across the entire sky and therefore a larger common ground to transfer knowledge between surveys.

5.5. Classification of emission line sources

Among the algorithms devoted to the analysis of XP spectra for *Gaia* DR3, the ESP-ELS Apsis module is designed to identify six classes of ELS: Be stars, Herbig Ae-Be stars, T Tauri stars, active M dwarf stars, Wolf-Rayet (WR) stars, and planetary nebulae (PNe; Fouesneau et al. 2023). The selection and classification is based on the use of two Random Forest classifiers trained on libraries of synthetic spectra as well as on observed *BP*/*RP* data obtained for a sample of reference ELSs (see detailed description of ESP-ELS in online documentation). To study the extent to which ESP-ELS results can be reproduced using XP-based synthetic photometry, we chose a custom system, `ELS_custom_w09_s2`[21], which is illustrated in Fig. 34. This latter is composed of three narrow passbands with Gaussian shape and located at the rest frame wavelength of the Hβ, [OIII] 5007, and Hα lines. It is complemented with three passbands aimed at sampling the continuum in spectral regions adjacent to the lines of interest and with minimal contamination from other emission lines, and by the wide SDSS r and i bands. All the TCs have $Rf \geq 1.4$ (see Appendix B).

In order to have a reference sample, we extracted ELS from the SIMBAD[22] database and obtained a total of 1962 Be stars, 143 Herbig Ae/Be objects, 3704 T Tauri stars, 269 WR stars, and 593 PNe, while active M dwarfs are not considered in our experiment. We also selected 102 763 targets with no ELS classification and 196 801 targets randomly taken from the IPHAS catalogue, taken from Scaringi et al. (2018), with no overlap between them. All of these stars are labelled 'Other' and represent normal non-emitting stars. We then cross-matched the sources with EDR3 using the CDS x-matcher, and selected the closest target within 1.0″. The comparison between the classification provided by Simbad and that by ESP-ELS is shown in Fig. 35. The precision of ESP-ELS is excellent, between 87% and 99% in the different classes, except for the Herbig Ae/Be stars, for which ESP-ELS correctly classify only 25% of the predicted sources. Despite the good results, the number of ELSs predicted as NO-ELSs demonstrates the quite conservative approach adopted by ESP-ELS; there are 5124 objects that are labelled as non-emitters, whereas these objects are ELSs according to SIMBAD.

[21] This newly defined system is included in the list that can be used to get XPSP by means of GaiaXPy (Sect. 6.1).
[22] http://simbad.u-strasbg.fr/simbad/

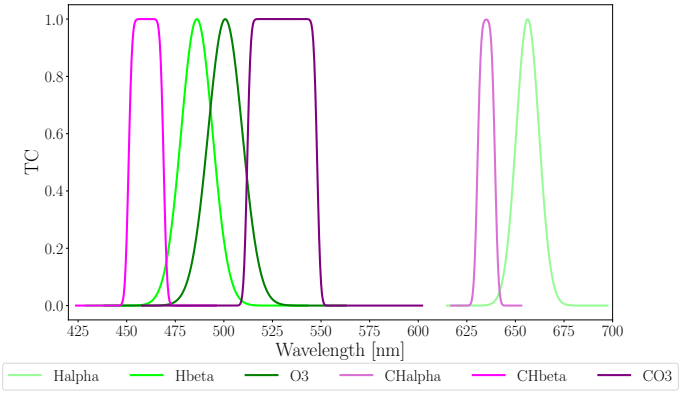

Fig. 34. ELS_custom_w09_s2 normalised transmission curves.

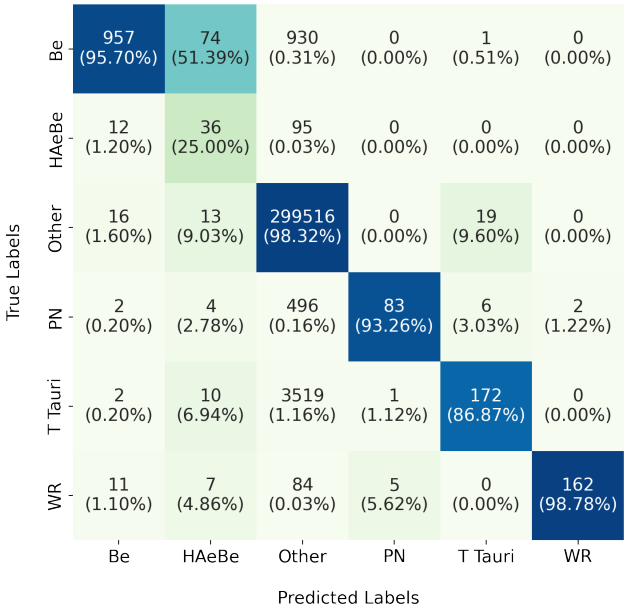

Fig. 35. Confusion matrix between ESP-ELS classification (predicted label) and Simbad (true label). For each class, the percentages refer to the fraction of true positives with respect to the total number of objects predicted by ESP-ELS for such a class (precision).

The following validation datasets were selected in order to cross-validate ESP-ELS classification results and, at the same time, demonstrate the classification capabilities of the chosen photometric system: (i) the selection of ELS described above, which add up to a total of 6671 objects; and (ii) the 196 801 IPHAS targets also described above, representing non-emitting stars (IPHAS sample, hereafter). Specifically, we wish to decipher the degree to which a classification based on narrow-band XPSP reproduces the results by ESP-ELS. For simplicity, we limit to the classification between ELS and non-ELS.

We combine a supervised method to classify the objects, namely Random Forest, with an unsupervised algorithm, t-SNE (van der Maaten & Hinton 2008), to group and picture the classification results. We also show two colour–colour diagnostic plots to visualise them. Three experiments were performed on different inputs:

1. All filters in `ELS_custom_w09_s2` synthetic photometry.
2. `ELS_custom_w09_s2` synthetic photometry except bands for Hβ, O3, and their respective continua.

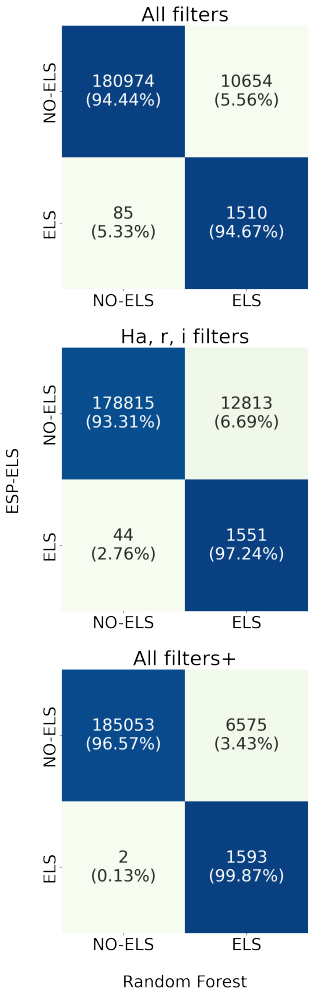

Fig. 36. Confusion matrices obtained using a Random Forest algorithm to separate between ESP-ELS emitting and non-emitting objects for experiments 1, 2, and 3 (see text for details). For each class, the percentages refer to the fraction of true positives with respect to the total number of objects predicted by ESP-ELS for such a class (recall).

3. `ELS_custom_w09_s2` synthetic photometry plus information from several band combinations: r–Hα, $r - i$, Hα–Hαcont, and Hβ–Hβcont.

We divided the objects into a training set composed of 5124 ELSs (labelled as non-emitters by ESP-ELS, but found to be true emitters in Simbad) and the same number of non-ELSs randomly taken from our IPHAS sample. Once trained, Random Forest was tested on the remaining ESP-ELS emission line stars (1595 objects) plus the remaining IPHAS objects. The confusion matrices obtained for experiments 1, 2, and 3 are shown in Fig. 36. In this case, the fractions reported in the confusion matrices are not the *precision* (the number of true positives divided by the number of objects predicted in that class) as in Fig. 35, but the *recall*, that is, the fraction of predictions matching the classification taken as 'truth'; in this case the ESP-ELS classification[23].

The confusion between classes is below 7.1% in both emitting and non-emitting objects. This indicates that all the tested combinations of synthetic passbands are well suited for the classification of ELSs. By including the Hβ and O3 passbands, the number of false positives (FPs) diminishes (from 6% to 2.8%)

[23] Adopting the notation introduced below, precision = TP/(TP + FP), and recall = TP/(TP + FN).

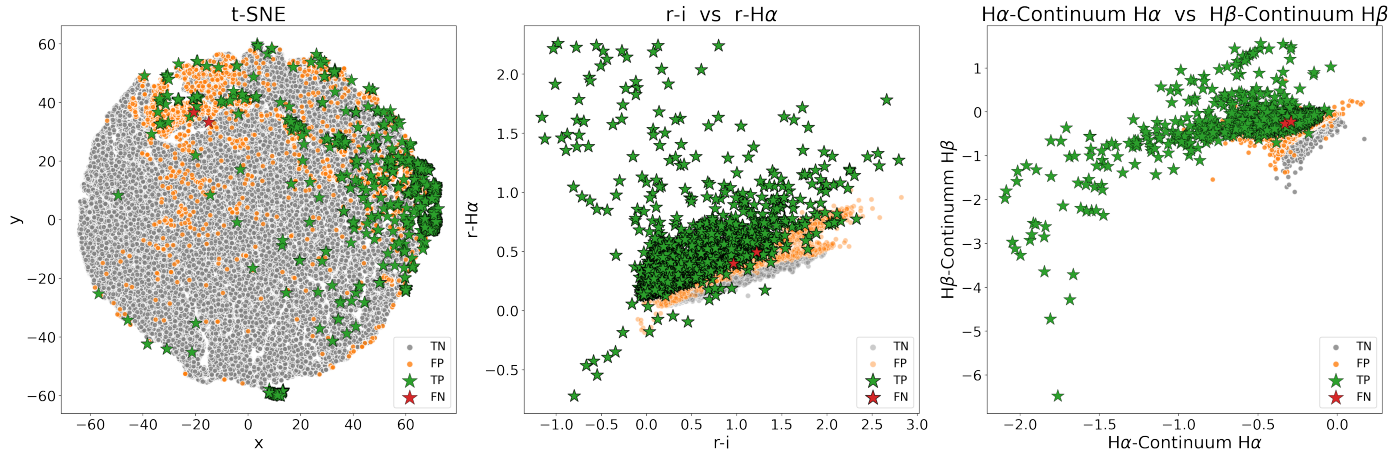

Fig. 37. t-SNE and colour–colour diagrams representing the sample of emitting and non-emitting stars, classified using a Random Forest algorithm on XP synthetic photometry (experiment 3). Legend as follows: TP: true positives; TN: true negative; FP: false positive; FN: false negative.

but the number of false negatives (FNs) increases (from 5.5% to 7.1%). The best classification results are obtained in experiment 3, where only two ELS are predicted as non-ELS, while keeping the number of FNs to only 3.5%.

Subsequently, we applied the t-SNE algorithm to the validation data, obtaining a 2D representation of the whole sample. t-SNE is an unsupervised algorithm, and does not use the labels to group the data, which are clustered according to the similarity of the XPSP fluxes. Once the clustering is done, it can be visualised using the labels (true negatives (TNs), FNs, FPs, and true positives (TPs)), which are obtained with the Random Forest for experiment 3, the one with the highest score in the confusion matrix. The results are shown in Fig. 37, where we also show two different colour–colour diagrams. Figure 37 is clearly dominated by TNs, with high confusion with TPs in the same area. Colour–colour diagrams are better suited to distinguishing the regions corresponding to each of the object classes.

In conclusion, through simple machine learning experiments and using both supervised (Random Forest) and unsupervised (t-SNE) algorithms, we show that the synthetic photometry in the system `ELS_custom_w09_s2` obtained from the *Gaia* XPSP is adequate to separate stars with emission lines from those that do not emit with a reliability that reproduces that achievable by the XP spectra themselves by the ESP-ELS module with errors below 3.5% for FNs and as low as 0.1% for FPs. The ability to go further and separate different classes of ELS objects strongly depends on the possibility to train the algorithms with sufficiently representative sets of each class and to use additional passbands as a possible way to improve the performance.

6. Products

6.1. How to get synthetic photometry in your preferred system

Synthetic photometry in all the photometric systems used throughout this paper can be generated from the *Gaia* DR3 XP spectra served by the archive[24] via Datalink (see Sect. 4 in De Angeli et al. 2023, for further instructions). The GaiaXPy[25] Python package offers several utilities to help users to maximise the potential of *BP* and *RP* spectra. The generation of synthetic photometry in a number of predefined photometric systems is one of the available functionalities. This is achieved by a simple matrix multiplication of the array of coefficients defining the mean spectra by a design matrix which is generated taking into account the specific photonic TC. Contributions from both *BP* and *RP* spectra in the case of filters spanning the range covered by both are taken into account (Montegriffo et al. 2023). Colour corrections for the UV bands of some of the standardised systems (see Sect. 2.2.2) and uncertainty correction factors (see Sect. 2.1) are also optionally available. To obtain standardised photometry, the properly tweaked passbands must be used (see Sect. 2.2.1), being denoted with `_STD` in their name.

GaiaXPy allows synthetic photometry to be generated in any of the available photometric systems or in a list of those in a single call. Users can either provide a list of `source_id` or input the XP spectra as downloaded from the *Gaia* archive in their continuous representation and in all file formats currently offered for their download. For updated and detailed instructions, readers are referred to the package documentation.

New photometric systems can be added to those already available in the latest release of GaiaXPy (see the GaiaXPy web page). However, synthetic photometry in any system can also be obtained from EC XP spectra in the usual way (Eqs. (1)–(5); Sect. 2) by any user of the *Gaia* archive, without the need for computing new basis functions.

6.2. The Gaia Synthetic Photometry Catalogue

To make XPSP more readily available in the most widely used photometric systems, we produced the *Gaia* Synthetic Photometry Catalogue (GSPC), which includes the vast majority of the approximately 220 million stars with XP spectra released in *Gaia* DR3. We limited the content of the GSPC to the sources brighter than $G = 17.65$ mag, thus excluding most of the sources in the special catalogue of WDs (which is treated separately below), and unresolved galaxies and quasars (included into the unresolved galaxy catalogue (UGC) and quasi-stellar objects catalogue (QSOC) of *Gaia* DR3, respectively; Gaia Collaboration 2023b). The catalogue will be accessible and queryable through the *Gaia* Archive (table `gaiadr3.synthetic_photometry_gspc`). Examples of queries are provided in Appendix F. GSPC is focused on wide-band photometry and is limited to standardised systems.

[24] https://gea.esac.esa.int/archive/
[25] https://gaia-dpci.github.io/GaiaXPy-website/

Table 5. Summary of the GSPC content for each passband.

Passband	Present	Mag range	Validated
U_{JKC}	32835800	2.22, 18.97	32279743
B_{JKC}	191343258	2.96, 20.31	160437248
V_{JKC}	217577173	3.10, 20.58	206285205
R_{JKC}	218861537	2.59, 19.99	206329396
I_{JKC}	218910521	1.98, 19.14	206346825
u_{SDSS}	37990533	3.07, 19.33	21965164
g_{SDSS}	210697330	2.89, 20.55	191247211
r_{SDSS}	218262272	2.85, 20.24	194747198
i_{SDSS}	218890040	2.46, 19.78	194853547
z_{SDSS}	218840583	1.86, 18.78	194788330
y_{PS1}	214043127	1.12, 18.48	187461656
$F606W_{ACS/WFC}$	218549069	2.81, 20.42	172587968
$F814W_{ACS/WFC}$	218919373	1.91, 18.95	172588424

Notes. The parameters provided are the number of sources with synthetic photometry available in the catalogue, the magnitude range covered and the number of sources that are within the ranges in magnitude and colour that are fully validated (i.e. that have the corresponding flag set to 1).

In particular, it includes standardised magnitudes, fluxes, and errors on fluxes for the following passbands:

- U_{JKC}, B_{JKC}, V_{JKC}, R_{JKC}, I_{JKC},
- u_{SDSS}, g_{SDSS}, r_{SDSS}, i_{SDSS}, z_{SDSS},
- y_{PS1},
- $F606W_{ACS/WFC}$, and $F814W_{ACS/WFC}$.

We decided to include only y_{PS1} from the PS1 system to avoid the redundancy implied by two different but very similar versions of the same set of magnitudes (*griz*). Moreover, the standardisation of SDSS performed here is more extensive and robust than what we achieved for PS1 magnitudes.

In addition to the XP synthetic photometry listed above, the GSPC contains: *Gaia* DR3 `source_id`, allowing a direct cross-match with other catalogues in the *Gaia* archive by means of `JOIN` ADQL queries, the quality parameter $C^\star$ (Riello et al. 2021), which can be used to select the sources with the most reliable photometry (but see also Sect. 7), a flag for each passband (`Xflag`, where `X=Ujkc,Bjkc,...`), which has a value of 1 if the $G_{BP}-G_{RP}$ colour and G magnitude of the considered star are within the ranges where standardisation and validation have been performed. In practice, the `X` magnitude of a source with `Xflag=0` should be considered as an extrapolation of the adopted standardisation.

To keep only good-quality measurements, we adopted a unique criterion based on S/N for all the magnitudes in all the systems. A given source has valid photometry in the passband `X` only if

$$\texttt{XFlux/XFluxError > 30.0}, \tag{21}$$

that is, the S/N in that passband is higher that 30. As can be clearly appreciated from Table 5, this constraint has a modest effect on the number of sources with valid photometry for all the considered passbands except for U_{JKC} and u_{SDSS}. In these passbands, the sample with valid measures is reduced to $\lesssim$17% of the entire content. As a reference, the next most affected passband is B_{JKC}, for which the same constraint leads to valid magnitudes for $\simeq$87% of GSPC sources. There are 30 220 sources with XP spectra in DR3 and $G < 17.65$ but without a single GSPC magnitude satisfying the $S/N > 30$ criterion; these are therefore not included in the final catalogue. It turns out that the overwhelming majority of them are very red AGB stars, possibly carbon stars. Most of them are classified as long-period variables (`in_vari_long_period_variable=True` in `dr3.vari_summary`), and 352 of them are classified as carbon stars (`spectraltype_esphs==CSTAR` in `dr3.astrophysical_parameters`).

As already anticipated in Sect. 3.3, the $S/N > 30$ selection criterion imposes a strong colour bias on UV magnitudes. Considering the subsample of all GSPC sources with Galactic latitude $|b| > 50°$ (Galactic Caps sample), while there are stars with valid U_{JKC}/u_{SDSS} magnitudes as red as $G_{BP}-G_{RP} \simeq 3.0$ mag, 95% of those with valid U_{JKC} have $G_{BP}-G_{RP} \leq 1.16$ mag and 95% of those with valid u_{SDSS} have $G_{BP}-G_{RP} \leq 1.18$ mag.

As a first glance at the quality of GSPC photometry, in Fig. 38 we show the JKC $U-B$ versus $V-I$ colour–colour diagram of the Galactic Caps sample introduced above for the entire sample (left panel) and for the best-quality subsample with $|C^\star| < 0.05$, containing about 87% of the sources (right panel). The high-latitude selection is especially useful as it minimises the effect of blending and/or contamination and makes the effect of interstellar reddening negligible. In the left panel, some remarkable loci are labelled (similarly to Fig. 22 in Ivezić et al. 2007). We note that a significant residual population of unresolved galaxies and QSOs brighter than $G = 17.65$ is included, some of them with $U-B$ colours far exceeding those of the bluest bona fide stars. This is likely due to a combination of two main factors: first, the spectrum of some of these sources may have a significant non-thermal component (from active nuclei, nebular emission, etc.), and, second, some of them may be partially resolved, thus making XPSP not fully reliable. The 'blue contaminants' class is a mixture of source types including, among others, significantly blended stars, compact blue sources in relatively nearby galaxies (young stars clusters, stellar nuclei, HII regions), and distant compact blue galaxies. It is interesting to note that most of these non-stellar sources are efficiently removed with a simple cut in $|C^\star|$, leaving in the left panel of Fig. 38 only well-defined stellar loci and a compact clump of truly point-source, bright QSOs.

The GSPC is intended to provide accurate and precise all-sky photometry down to $G = 17.65$ mag, with the limitations described above, in Sect. 2.2, and in Sect. 7, and is by no means a complete sample. Strong colour- and magnitude-dependent biases are unavoidably affecting the sample, induced by the selection criteria on the quality of the photometry. Moreover, the stellar populations sampled, the degree of crowding, and, consequently, the fraction of stars with excellent photometry, changes with position in the sky, depending on the mix of Galactic components encountered along the line of sight as well as on the amount of interstellar extinction[26]. Figure 39 gives overview examples of (i) the kind of selection bias at work (panel a), (ii) the effects of selection on the $C^\star$ parameter (panel b), as an example of a mean for additional cleaning of the sample, and (iii) the sensitivity of colour–colour diagrams to astrophysical parameters (panels c and d; parameters from from GSP-Phot Andrae et al. 2023).

Finally, to give an idea of the diagnostic power made available by GSPC (and by XPSP in general), in Fig. 40 we present a colour–colour diagram of the Galactic Caps sample obtained

[26] Please note that the cuts on magnitude and on the minimum number of *BP* and *RP* observations imposed for the release of XP spectra makes the footprints of the *Gaia* scanning law clearly visible in maps of GSPC sources.

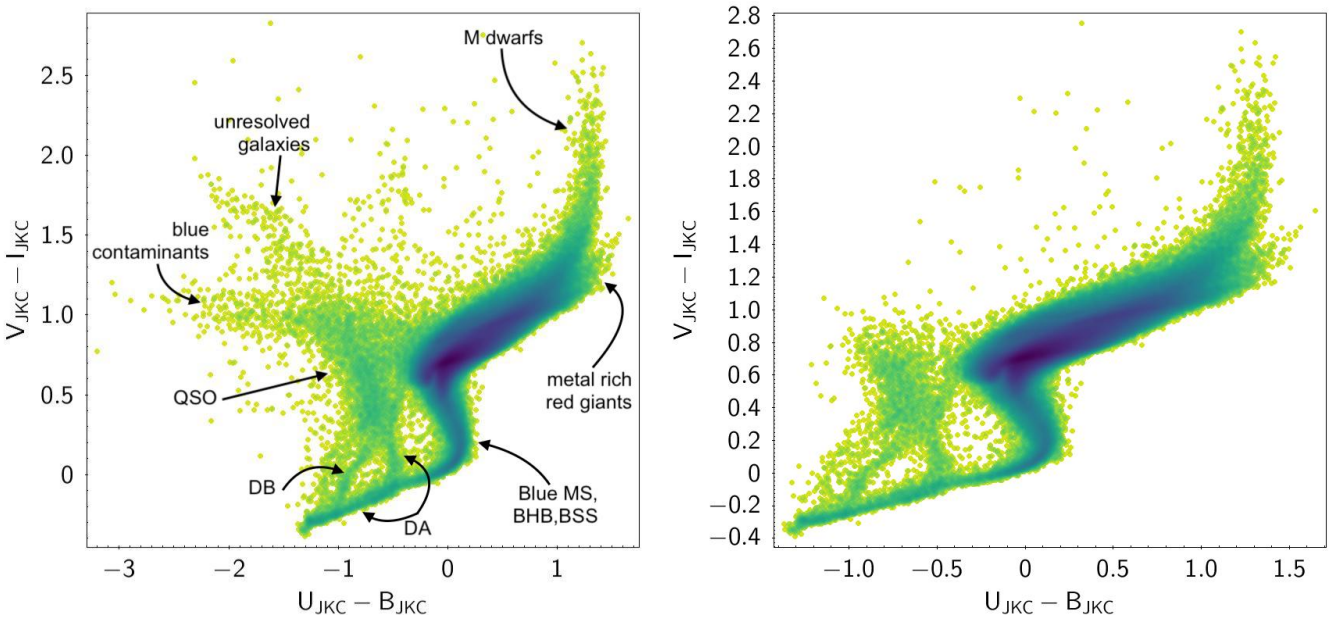

Fig. 38. $U - B$ vs. $V - I$ colour–colour diagram for the Galactic Caps subset of the GSPC ($|b| > 50°$). *Left panel*: all sources, with labels for remarkable loci (2 025 048 sources with valid photometry in all the involved passbands). *Right panel*: subset with $|C^\star| < 0.05$ (1 985 565 sources).

by mixing magnitudes from two of the four photometric systems included in the GSPC.

The diagrams display many well-defined features, suggesting a great potential to select various classes of sources. In spite of the $|C^\star| < 0.05$ selection imposed to remove most non-stellar non-best-quality sources, the diagram includes more than 95% of the sources of the original sample.

6.3. The synthetic photometry catalogue for white dwarfs

White dwarfs are important objects, and as well as meriting their own dedicated investigation, they can be used as tools to explore other areas of astrophysics. For example, there is strong evidence that many WDs are accreting the remains of extrasolar planetary systems, which provides the only means of measuring their bulk composition. Furthermore, measured ages for the coolest known WDs can provide a limit to the age of the Galactic disc. Many such studies require knowledge of the spectral type of the WDs in question, and whether or not they have H- or He-rich atmospheres. As the number of discoveries of WDs grows, increasing numbers of spectroscopic observing campaigns are carried out to provide this information. The Sloan Digital Sky Survey (SDSS, Ahn et al. 2012) has produced the largest spectroscopic catalogue of WDs so far (e.g. Kleinman et al. 2013), a data set that has allowed classification of approximately 10 000 WDs, the largest statistical sample of such stars prior to the publication of the *Gaia* DR2 and *Gaia* EDR3 catalogues (Gaia Collaboration 2018a, 2021b). The quality- and distance-selected samples of Gaia Collaboration (2018b, 2021a) each contain approximately 20 000 to 25 000 WDs and the works of Gentile Fusillo et al. (2019, 2021) indicate that there might be as many as roughly 300 000 in the whole *Gaia* catalogue. However, obtaining follow-up spectroscopy to classify all these candidates will be an enormous challenge and is not likely to be feasible using the currently available telescope resources.

The *Gaia* data release 2 (DR2) H-R diagram presented by Gaia Collaboration (2018b) shows a clear WD cooling sequence

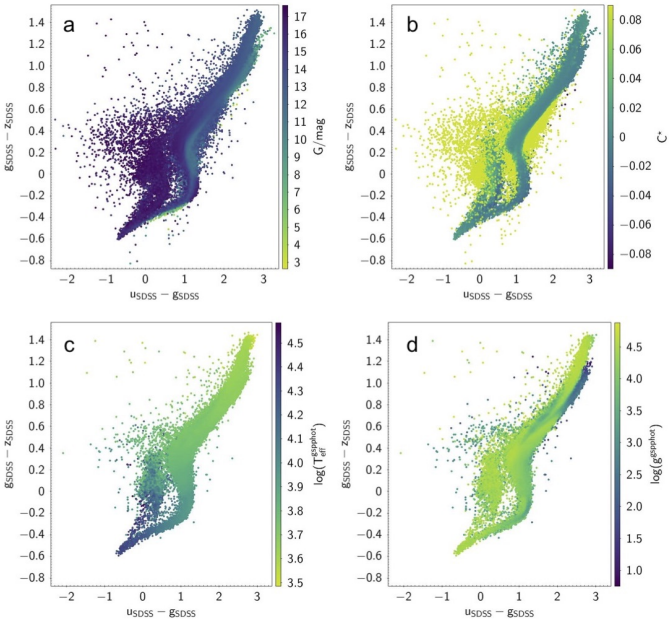

Fig. 39. $u - g$ vs. $g - r$ colour–colour diagram for the Galactic Caps subset of the GSPC ($|b| > 50°$; 2 003 727 sources having valid photometry in all the involved passbands), colour coded according to different parameters. *Panel a*: G magnitude; *panel b*: $C^\star$; *panel c*: log $T_{\rm eff}$ from GSP-Phot; *panel d*: log g from GSP-Phot.

and a degree of separation between the populations of H-rich (DA) and He-rich (DB) stars. However, while the WDs have a narrow range of masses, there is a significant overlap between the H- and He- groups over much of the parameter space. The *Gaia* G, $G_{\rm BP}$, and $G_{\rm RP}$ integrated bands are broad in order to provide maximum sensitivity and the best possible photometric accuracy, and this limits the ability to distinguish between WDs of different spectral types. Wide- to narrow-band synthetic photometry generated from the *Gaia* XP spectra can be used to mimic the narrower band photometry available from surveys

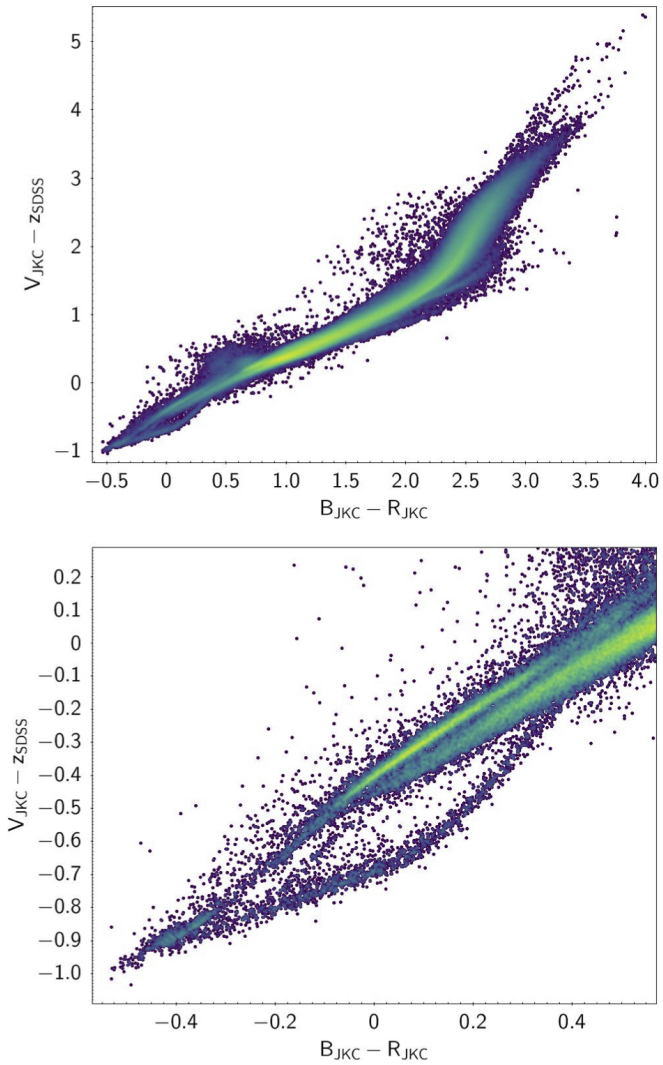

Fig. 40. Colour–colour diagrams for the Galactic Caps subset of the GSPC ($|b| > 50°$), with colours obtained by mixing magnitudes from the JKC and SDSS photometric systems. To highlight the stellar loci more clearly, we included only stars with $|C^\star| < 0.05$ (5 968 495 of the 6 266 882 GSPC sources in the Galactic Caps sample). *Upper panel*: overall colour–colour diagram. *Lower panel*: zoom into the highly structured blue region hosting sequences of DA and non-DA WDs, hot subdwarfs and extreme horizontal branch stars, blue horizontal branch stars, and so on, better demonstrating the level of detail emerging in these diagrams.

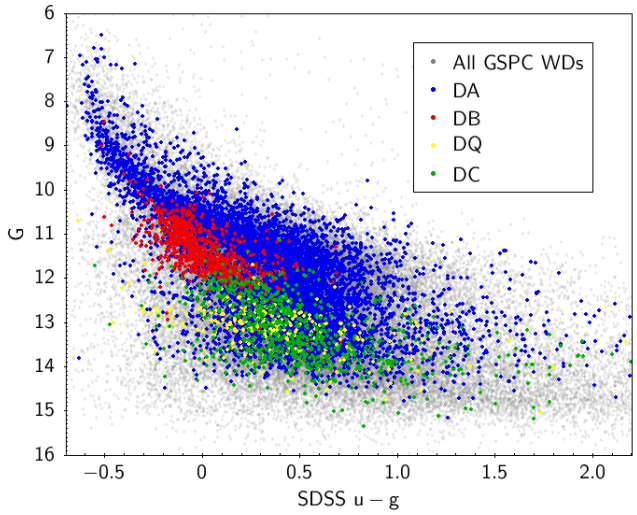

Fig. 41. Synthetic $u - g$ colour vs. absolute G-band magnitude diagram for white dwarfs in the GSPD-WD catalogue (grey). Data points are colour-coded according to SDSS spectral type where known: blue = DA, red = DB, green = DC, yellow = DQ.

such as SDSS, allowing the diagnostic power to be applied to the larger number of WDs present in the *Gaia* catalogue.

To test and illustrate this potential, we constructed a catalogue of about 100 000 WDs initially drawn from the *Gaia* EDR3 data release, for which we have generated synthetic photometry in JKC, SDSS, J-PAS, and J-PLUS bands. This well-defined sample of WDs is designed to span the complete range of colours and magnitudes occupied by WDs. All the objects have a high probability of being a WD by virtue of their location in the H-R diagram. We followed the methodologies applied by Gentile Fusillo et al. (2019) and the GCNS (Gaia Collaboration 2021a). The selection criteria are designed to remove contaminants whilst retaining as many high-probability WDs as possible. The sample extends to greater distance than the GCNS, and yields 100 786 WDs, a factor five increase compared to that catalogue. Specifically, the following H-R diagram location and quality cuts were applied:

- Equations (1)–(9) detailed in Gentile Fusillo et al. (2019),
- astrometric_excess_noise ≤ 5,
- phot_bp_mean_flux_over_error ≥ 20,
- phot_rp_mean_flux_over_error ≥ 20,
- parallax/parallax_error ≥ 10,
- phot_g_mean_flux_over_error ≥ 20,
- log(parallax/parallax_error) $< -1.56(\log(10^3/\text{parallax}) - 3.17) + 0.96$.

The majority of the stars in the sample have $G < 19$ mag, but about 30% are fainter. The effective G-band magnitude cut-off is $\approx$20 mag.

We derived synthetic photometry in SDSS, JKC, J-PLUS, and J-PAS systems for the full set of available WDs in the sample, which we designate the *Gaia* Synthetic Photometry Catalogue for WDs (GSPC-WD), which is published with this paper (see below, for the actual contents of the published table). Among these objects, 9758 have WD subtypes assigned by SDSS observations. Figure 41 shows absolute G-band magnitude plotted against the synthetic SDSS $u - g$ colour for these stars, indicating the main classifications. The SDSS photometry gives a much better separation between the DA and DB WD spectral types than the *Gaia* photometry (see Fig. 13 of Gaia Collaboration 2018b). The DB stars also occupy a different region of the diagram compared to DC and DQ, but their ranges overlap substantially, and they also overlap with that of the cooler DAs. Therefore, the synthetic magnitudes for bands that are narrower than G-band, G_{BP}, and G_{RP}, provide a potential classification mechanism for all WDs in the *Gaia* catalogue.

The choice of $u-g$ as an indicator of H-atmosphere DA spectral type compared to He-atmosphere DB WDs is related to the relative wavelengths of the bands compared to the Balmer jump at 364.5 nm, where the H Balmer series of lines converges. Compared to the DB WDs, the flux of DA WDs is suppressed shortward of this wavelength, making the stars appear redder, as seen in Fig. 41. In principle, there are many potential passband combinations available that may provide better or similar discrimination between DA and non-DA stars. For example, narrower passbands will allow better discrimination than wider ones, as

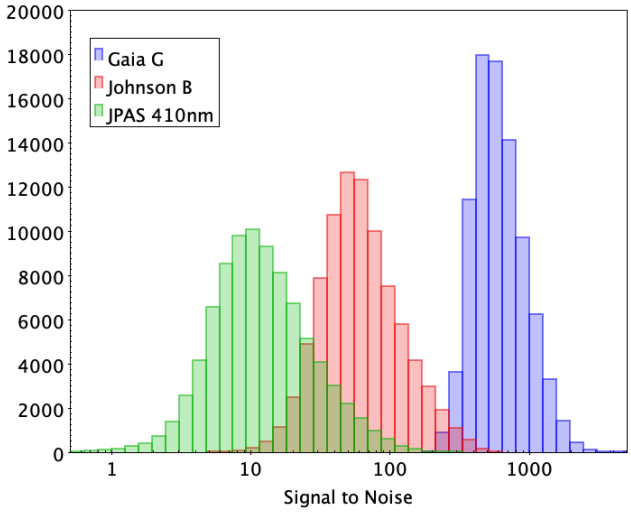

Fig. 42. S/N distributions for the stars in the GSPC-WD sample in three different filter bands: blue – G-band, red – synthetic Johnson B, and green – synthetic J-PAS 410 nm.

discussed above. However, finer subdivision of the spectroscopic data reduces the S/N of individual bands. This is illustrated in Fig. 42, which compares the S/N (flux over flux error) for the G-band, synthetic Johnson B, and, as an example of the narrowest bands, J-PAS 410 nm. The Johnson B band has approximately one-tenth of the S/N of G-band and the J-PAS 410 nm band one-fifth of Johnson B.

Whichever combination of filter bands is used to attempt the classification of the WDs, it is not straightforward to separate star types where their parameter space overlaps. Furthermore, it is a complex exercise to simultaneously use more than one colour–magnitude diagram to define the locus of particular spectral types. In trying to create 'clean' samples of single WD classes for population studies, we need an objective method for carrying out the classification to distinguish among hydrogen type WDs (DA) and other types of WDs among these intrinsically faint sources. A Random Forest algorithm allows us to make use of all the available photometry to carry out this task and determine a classification probability for DA WDs. We used the SDSS dataset of 9758 WDs with known classifications to train the Random Forest algorithm to distinguish between DA and non-DA spectral types. For the DA selection, we included all SDSS subtypes whose main type is 'DA' in the classification scheme[27]. Among all the WDs with known subtypes, we were able to select 7567 DA and 2191 non-DA stars to be used to train or test the Random Forest algorithm. For training, we selected 1500 DA and 1500 non-DA, using the rest for testing purposes. The input parameters used to perform the classification included all the SDSS, Johnson, J-PAS, and J-PLUS synthetic magnitudes, their uncertainties, and other information from *Gaia* (parallaxes, proper motion, integrated magnitudes and their uncertainties).

Using the Random Forest classification, we can use the obtained probabilities of being a DA to create a clean DA-type WD sample (Table 6). For example, if we use only sources with probability larger than 0.7 of being a DA, derived using J-PAS filters, only 0.11% non-DAs will contaminate our sample of selected sources.

[27] This includes the following subtypes: "DA","DA(He)","DA(He)Z", "DA+BD","DA+M","DA+M3","DA+M4","DA+M5","DA+M7", "DA+M:","DA+Me","DA:","DA:DC","DAB","DAB+M","DABH", "DAZ","DAE","DAH","DAH:","DAO","DAQ","DAQ:","DAZ", "DAZ:","DAZB","DAZE:","DAZH:","DAe","DA+DB","DA:DC:".

Table 6. Percentage of non-DA sources contaminating our sample if selecting sources with probability of being a DA larger than x when using different input passbands for classification.

Input	$x = 0.5$	$x = 0.6$	$x = 0.7$
SDSS	2.45	0.86	0.30
J-PLUS	1.43	0.55	0.27
J-PAS	0.77	0.26	0.11
Source coefficients	0.50	0.15	0.03

Once the algorithm has been trained and validated, we can apply it to all the white dwarfs in the GSPC-WD catalogue, including those where an SDSS classification is not available. Figure 43 shows the probability distribution for all four cases studied (SDSS, J-PLUS, J-PAS and source coefficients). Based on our results, the narrower the pass bands, the better the classification (increasing their probabilities and obtaining a less centred distribution), improving also when more pass bands are considered, covering the whole wavelength range. Nevertheless, it can also be seen that the best results are obtained when using the *BP* and *RP* coefficients representing the spectra, rather than the synthetic photometry.

When analysing the colour distribution of sources with SDSS types available to train our algorithm we see that 96% of the sources fall in the range $G - G_{\rm RP} < 0.4$ mag. For this reason it is expected that the algorithm is not working optimally for colours outside this range. In order to verify this, we show only those sources with $G - G_{\rm RP} < 0.4$ mag in an overlapped distribution in Fig. 43. Indeed, sources with larger values for $G - G_{\rm RP}$ are those located at intermediate probabilities, and this method is not able to properly classify them. Not all WDs in the sample have a complete set of JPAS magnitudes for classification, as some sources are too faint to generate significant magnitude measurements. Therefore, the total number of WDs classified by the Random Forest algorithm is 86 783, to which we can add the 9758 WDs already classified by SDSS: a total of 96 541 WDs.

The usefulness of the DA/non-DA classification scheme can be illustrated by considering the G-band versus Johnson $B - V$ colour–magnitude diagram (left hand panel of Fig. 44). The distribution is colour coded by the probability of a WD being a DA. The DA and non-DA cooling tracks appear to be clearly separated by the $B - V$ colour. Similarly, the $B - V$ versus $V - R$ colour–colour diagram (right hand panel of Fig. 44) shows very good isolation of the DA and non-DA components. However, when we examine the distributions of DA and non-DA classifications separately, we see that there is considerable overlap of these in the parameter space of the colour–magnitude diagram (Fig. 45). The figure shows all WDs with probability of being a DA above 0.5 (blue), with a non-DA contamination fraction of 0.77% (Table 6). Overlaying this distribution are those WDs with probability of being a DA of less than 0.3 (cyan). This shows the great difficulty in separating out DAs and non-DAs on the basis of a cut in any colour–magnitude diagram and underlines the importance of the Random Forest classification method.

In conclusion, we demonstrate that synthetic photometry for a range of standard systems can be used to classify white dwarfs in the *Gaia* catalogue into DA and non-DA types. However, we note that better results are achieved using the coefficients of the *BP* and *RP* spectra, without the need to compute the

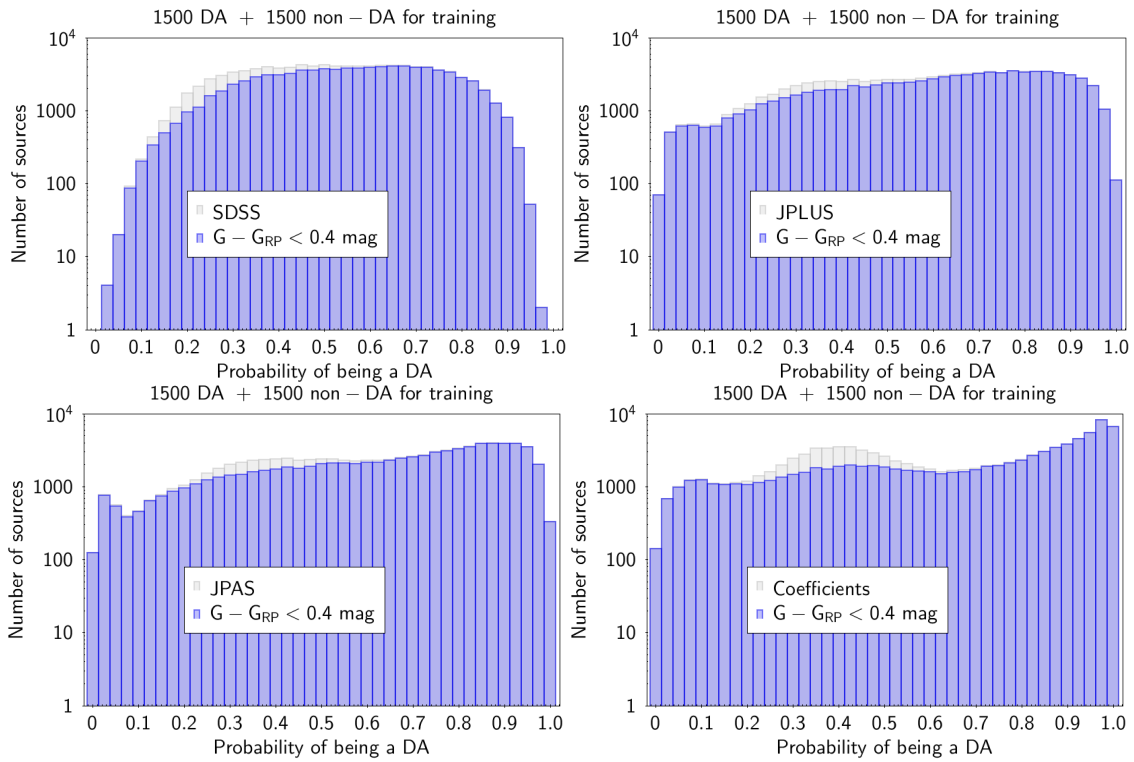

Fig. 43. Probabilities obtained for all classified WDs when using only SDSS (*top-left*), J-PLUS (*top-right*), and J-PAS (*bottom-left*) pass bands and the *BP* and *RP* source coefficients directly (*bottom-right*). In blue, the same histogram when we filter the reddest sources (keeping only those with $G - G_{RP} < 0.4$ mag), as they are not covered by the training dataset and lower output probabilities are expected.

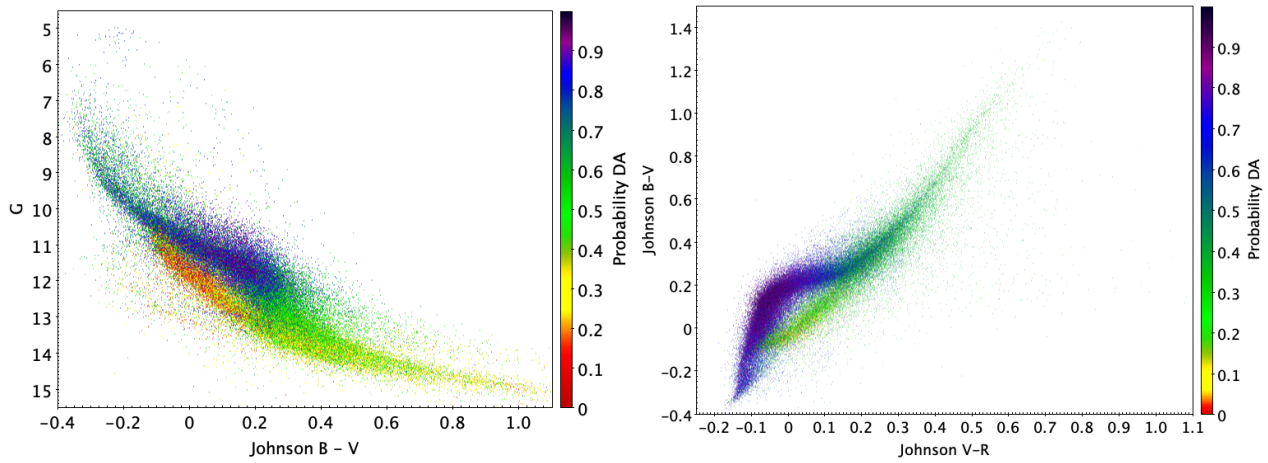

Fig. 44. (*left*) *Gaia* absolute G magnitude vs. $B - V$ colour–magnitude diagram for the GSPC-WD sample colour-coded with the probability of a WD being a DA. (*right*) *Gaia* $B - V$ vs. $V - R$ colour–colour diagram for the GSPC-WD sample colour-coded according to the probability of a WD being a DA.

synthetic photometry. Nevertheless, the differences are small and, although our classification is not perfect, a catalogue of the synthetic photometry for our sample of *Gaia* white dwarfs provides a useful resource that can be applied to generating samples of white dwarf types without the need for further computation. As we use J-PAS synthetic photometry to classify white dwarfs in *Gaia* DR3, there is a strong prospect for the real J-PAS survey (Benitez et al. 2014) to be used in a similar way. Indeed, the J-PLUS data have been used to classify and parameterise approximately 6000 WDs (López-Sanjuan et al. 2022). Clearly, this is a much smaller number than the WDs included in this work, but the S/N of the observations is potentially greater than we were able to achieve with the *Gaia* DR3 data. Therefore, the full J-PAS and J-PLUS surveys could provide valuable complementary data for analysis of the GSPC-WD catalogue.

We have made the GSPC-WD synthetic photometry available as a stand-alone catalogue[28], including SDSS, JKC, and J-PLUS XPSP and the DA classification probability. The photometry of the individual J-PAS bands used in the Random Forest analysis is not included because of their low S/N. For WDs classified in SDSS, a subset of which were used in the training and validation of the Random Forest algorithm, we also include the full SDSS classifications as a separate column in the GSPC-WD catalogue table. As can be seen from the example in Fig. 42,

[28] https://zenodo.org/record/6637717#.YqcREC8RpAY.

when the synthetic spectral bands are very narrow, a significant number of sources will have low S/N. Furthermore, at the edges of the *Gaia* spectral range, away from the peak of the effective area, this is also true for some stars in the wider bands included in the catalogue. In some extreme cases, there is no significant detection of the object. The Random Forest algorithm is only able to classify a WD when valid flux measurements are available for every photometric band we include in the analysis. Therefore, no classification is recorded in the catalogue when data for one or more bands is 'missing'. In total, 15 003 WDs from the total sample of 101 783 are not classified. For completeness, we have made all the flux measurements and corresponding magnitudes available for all objects in the GSPC-WD. Therefore, magnitudes and fluxes with very large errors up to several times the flux itself are included. However, where fluxes are negative, the magnitudes are not defined. When using the catalogue, appropriate S/N cuts are advisable for specific scientific objectives in order to ensure data quality.

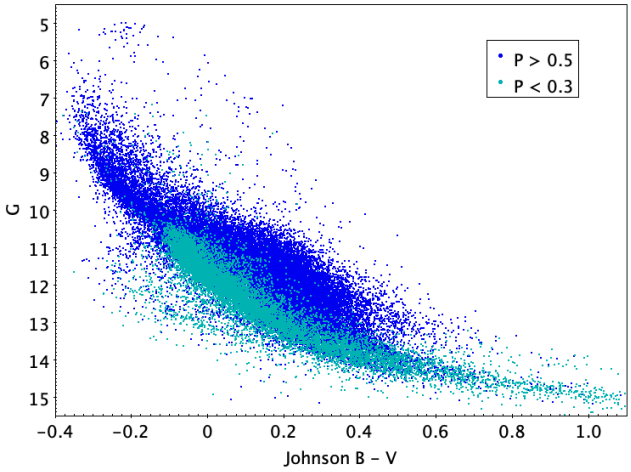

Fig. 45. (Blue) *Gaia* absolute G magnitude vs. $B-V$ colour–magnitude diagram for the GSPC-WD sample with probability of being a DA > 0.5. (cyan) *Gaia* absolute G magnitude vs. $B-V$ colour–magnitude diagram for the GSPC-WD sample with the probability of being a DA < 0.3.

7. Recommendations and caveats

In this section we provide some caveats and recommendations that can serve as guidelines for best use of the products described and provided here. It is important to be aware that, in spite of the huge effort made to check and verify XPSP, the results of which are only partially shown and discussed here because of obvious constraints on publishing space, the validation we provide is in any case partial, being unavoidably limited to high-quality reference samples that may not be perfect nor fully representative. In the discussion of the comparisons presented here, we focus almost exclusively on the known problems affecting XP spectra[29], as described in Montegriffo et al. (2023) and De Angeli et al. (2023), but in fact, some of the observed anomalies may be due to issues in the reference samples.

In any case, the users are invited to further validate the XPSP data they use, depending on their science goals and applications. The performances illustrated here should be considered in a statistical sense, and the individual magnitudes may still suffer from problems not traced by the available quality parameters.

We did not make extensive tests to verify whether Δmag distributions for a given system and/or reference set depend on the luminosity type of the considered stars (e.g. giants, dwarfs, WDs, etc.) or on the interstellar extinction. In general, the sets we adopted for validation and/or standardisation, while being predominantly composed of dwarfs, includes all types of stars. For example, we verified that, in the Landolt's sample, WDs do not show a different Δmag distribution as a function of colour with respect to other kinds of stars in the same colour and magnitude range, within the uncertainties. In Sect. 4.2 it is shown that, in the J-PAS and J-PLUS systems, XPSP has very similar performances for WD and normal stars, except for the UV passbands. In our experience the most problematic range in this respect is that of cool stars, especially M-type stars, where giants and dwarfs may also behave differently in response to tiny differences in the TCs. In the cases of the SDSS system, we explicitly checked that red ($1.0 < G_{\rm BP}-G_{\rm RP} < 3.5$) giants and dwarfs have compatible Δmag distributions, within ≃10 mmag (however, limited to K stars; see Appendix D for further discussion). The same is true for the JKC, albeit tested with a much smaller sample of red giants (Sect. 3.2).

In general, the accuracy of the standardised photometry presented here has not been tested against large variations in the interstellar extinction. Hence, in cases of highly reddened stars, XPSP should be used with caution. However, the analysis presented in Appendix D suggests that, at least in the considered case (red giants in the SDSS system), stars with extinction as large as $A_0 \lesssim 5.0$ mag have Δ mag virtually indistinguishable distributions from their low-extinction counterparts, where A_0 is the monochromatic extinction at $\lambda = 547.7$ nm as estimated by GSP-phot (Andrae et al. 2023).

We also note that the XPSP performance has not been tested, or only partially (see Sect. 3.5), in the presence of a significant degree of crowding or of a strong astrophysical background (see also the cautionary note at the end of Sect. 2.2.1). We are not aware of spatial variation of the systematic errors affecting XP ECS but we cannot exclude their existence. However, their amplitude should be very small, owing to the careful process of internal calibration of *BP* and *RP* spectra (Carrasco et al. 2021; De Angeli et al. 2023).

The main goal of this paper is to show the potential of XPSP, a new product available for the first time in *Gaia* DR3. We are confident that the astrophysical community will explore this potential much more extensively, seeking and extracting the greatest scientific return. Within the limits of our resources, we will be happy to support extensions of the available photometric systems (see Sect. 6.1). We stress again that standardised $U_{\rm JKC}$ and $u_{\rm SDSS}$ XPSP cannot provide an exact reproduction of the corresponding reference magnitudes because they lack the bluest part of the wavelength coverage. Moreover, in general, standardisation of any magnitude is strictly valid only in the colour and magnitude range and in the range of astrophysical parameters where the processes have been performed, the range covered by the adopted reference sample (see Sect. 6.2).

It is important to recall that the calibration of XP ECS and the instrument model used to get XPSP are best suited to dealing only with point sources. Synthetic magnitudes of extended or

[29] It is not necessarily easy to disentangle problems due to the process of external calibration (Montegriffo et al. 2023) and to the internal calibration of XP spectra (De Angeli et al. 2023). Here we generally consider colour trends as due to imperfections in the instrument model, and therefore associated to EC XPs. On the other hand, external calibration cannot be responsible for the trends with magnitudes, such as e.g., the hockey-stick effects or the blue dip, which is due to imperfection in the internal calibration process. Hopefully, both sides of the process should significantly improve in future data releases.

even marginally resolved sources may (and, in fact, should) be affected by systematic errors depending of their extension, their spectrum, and the width and wavelength range of the considered passbands. Also, the entire chain of *Gaia* data processing leading to XPSP is designed for single stars and calibrated on single non-variable stars: magnitudes of sources with relevant non-stellar components in their spectra, of variable sources, and of unresolved multiple stars are not expected to have accurate XPSP. However, this does not imply that their synthetic magnitudes, fluxes, and colours do not carry useful information on these sources.

Saturation of portions of XP spectra may occur in a variety of circumstances, depending on the magnitude, colour, and detailed spectral shape of the sources (i.e. presence of emission lines), with obvious effects on the accuracy of the derived XPSP. As a general rule of thumb, derived from the analyses by Riello et al. (2021), De Angeli et al. (2023), and especially Montegriffo et al. (2023), we can assume that XPSP should be free from saturation effects for $G \gtrsim 5.0$. XPSP from the *BP* spectral ranges are more easily affected, while reasonable photometry in the *RP* range should be possible up to $G \simeq 3.0$ in most cases. Finally, the performance of the internal calibration of *BP* and *RP* spectra for $G \lesssim 11.5$ is not as reliable as for fainter sources. The onset of different window classes and gate setups to extend the linear regime of the detectors up to $G \simeq 5.0$ and beyond makes the *Gaia* spectrophotometric system in this bright regime not perfectly matched with that established for $G \gtrsim 11.5$ (see De Angeli et al. 2023; Montegriffo et al. 2023, and referenced therein). For these reasons, the accuracy and precision of XPSP should be poorer at very bright magnitudes and, in general, above the $G \simeq 11.5$ limit, than for high-S/N measures below it.

A large number of parameters are available from the *Gaia* DR3 archive for all sources with XP spectra. Here, we provide a few suggestions for how to select the best data. Users will have to consider which ones are appropriate and at which level, depending on their science case.

- The renormalised unit weight error `ruwe` (available in `gaia_source`) can be used to clean a sample from cases showing photocentric motions due to unresolved objects, such as astrometric binaries. Some guidance on filtering based on this parameter is provided in Lindegren et al. (2021). The criterion `ruwe` < 1.4 retains about 93% of the sources with XP spectra in *Gaia* DR3.
- The corrected $G_{\rm BP}$ and $G_{\rm RP}$ flux excess factor C^* defined in Riello et al. (2021) and available from the GSPC table as `c_star` is useful to clean the dataset from objects affected by inconsistencies in the photometry in the various bands (G-band, $G_{\rm BP}$, $G_{\rm RP}$). These inconsistencies can be due to different source properties (e.g. in the case of extended sources) or systematic errors in the calibration procedures (e.g. in the case of residual background due to nearby bright sources). See Riello et al. (2021) for more details. The same paper (Sect. 9.4) provides a function reproducing the 1σ scatter for a sample of well-behaved isolated stellar sources with good-quality photometry. The criterion $C^\star < 1\sigma$ retains 79% of the sources, while a more generous $C^\star < 3\sigma$ retains 90% of the sources.
- The photometric errors can be used to define a variability proxy as $\sqrt{n}\,\sigma_{\rm f}/f$, where n is the number of observations and f and $\sigma_{\rm f}$ are the flux and its uncertainty in the G-band (Mowlavi et al. 2021). All required parameters are available from the `gaia_source` table. This can be used effectively to remove objects that vary in flux. A possible criterion could be defined selecting sources that have a variability proxy value within K sigma from the average value at a given magnitude: this would retain 95% of the sources for $K = 1$ and 99% of the sources for $K = 3$.
- Variable stars can be identified also using `phot_variable_flag` from the `gaia_source` table, while a classification of the candidate variables by type can be found in the `vary_summary` table.
- Finally, users may be interested in cleaning the dataset from objects affected by crowding. An assessment of the number of transits that contributed to the generation of the source spectra in *Gaia* DR3 and that were affected by a non-target source within the window (these cases are labelled blended) or by a nearby bright object (contaminated) is provided in the table `xp_summary` and in particular in the parameters `bp/rp_n_blended_transits` and `bp/rp_n_contaminated_transits`[30] (including the β parameter, used in Sect. 5.1). It should be mentioned that such assessment is based on the *Gaia* DR2 source catalogue. It is therefore expected that the crowding assessment may not be accurate in very dense regions due to the reduced completeness of the catalogue and in cases of sources with very small angular separation. The fraction of transits flagged as blended or contaminated can be used as an additional criterion to remove data affected by crowding.

Section 6.1 in De Angeli et al. (2023) provides more details on the XP spectral data available in the *Gaia* DR3 archive, instructions on how to download the data, and recommendations regarding the treatment of the data. For the purpose of generating synthetic photometry, we recommend using full, non-truncated XP spectra. Truncation has been introduced to remove spurious features in the spectra due to higher order bases fitting the noise in the observed data, particularly for faint sources or sources with a low number of observations. This is achieved by dropping coefficients that are consistent with being noise. When generating synthetic photometry by effectively integrating the spectrum in a given wavelength range, the precision of the result is not significantly improved by applying truncation. On the contrary, in the case of particularly narrow bands, truncation may introduce some systematic errors. See Sect. 3.4.3 in De Angeli et al. (2023) for more details. Appendix F shows a few examples of queries to create selections from the GSPC and to extract the corresponding parameters from the main table `gaia_source`.

8. Conclusions and perspectives for the future

We present a *Gaia*-DPAC product made available for the first time with *Gaia* DR3 that provides the possibility to obtain synthetic photometry in any passband for all the stars with published XP spectra, provided that the passband is entirely included in the XP wavelength range (330 nm–1050 nm), and that the FWHM of the passband is significantly larger than that of the *BP* or *RP* LSF at the considered wavelength ($Rf \geq 1.4$; but see Appendix B for a thorough discussion).

We show that wide-band photometry is reproducible within a few percent over wide ranges in magnitude and colour. We demonstrate this result for several widely used systems with good internal precision. The accuracy and precision decrease when considering medium- and narrow-band photometry; however, we show that even with measurements from this kind of passbands, performances are, at least, comparable with state-of-the-art ground-based observations, and fruitful scientific

[30] Please note that the `gaia_source` table contains equivalent counters applicable to the photometric data, i.e. integrated $G_{\rm BP}$ and $G_{\rm RP}$.

applications are possible. For example, the *Gaia* C1 system (Jordi et al. 2006) was brought into life by *Gaia* XPSP and we demonstrate its capabilities to deliver the astrophysical information, including stellar temperature, gravity, metallicity, and even α element abundance, an especially challenging task for the very low-resolution XP spectra (Gavel et al. 2021).

The residual shifts and trends affecting XPSP, which are mainly due to known systematic errors in the EC XP spectra, can be corrected down to millimag accuracy in some cases using suitable sets of external photometric standards as a reference, a process that we call standardisation. We performed the standardisation for the JKC, SDSS, PS1, and Strömgren systems, as well as for three wide passbands from two different HST systems. In addition, we demonstrate that XPSP is suited to calibrating narrow-band photometry for surveys designed to trace emission lines in stars.

We provide a few examples of scientific applications, demonstrating the performance of XPSP to trace multiple populations in globular clusters, classify emission line sources, and obtain metallicity estimates, also in the very metal-poor regime. The latter is a realm where the complementarity with the DPAC products directly derived from the analysis of XP spectra (GSP-Phot, Andrae et al. 2023) can be more fruitful. We show that by adopting reliable reddening values from external sources, dedicated photometric indices can give satisfactory performances.

Finally, we provide two publicly available catalogues for general use: (a) the *Gaia* Synthetic Photometry Catalogue (GSPC), queryable from the *Gaia* Archive, containing standardised photometry in 13 widely used wide passbands for ~220 M stars with $G < 17.65$ all over the sky (table `gaiadr3.synthetic_photometry_gspc`), and (b) the *Gaia* Synthetic Photometry Catalogue for White Dwarfs (GSPC-WD), publicly available as a stand-alone catalogue, containing synthetic photometry in many bands and DA/non-DA classification for a sample of approximately 100 000 WDs down to $G \simeq 20.0$.

We demonstrate that XPSP can provide precise space-based all-sky photometry in any optical band, with performances depending on the passband width and wavelength range. Furthermore, XPSP may significantly impact the photometric calibration of existing observations and the design of planned surveys (see, e.g. Sect. 4.4). For the first time it provides extensive means to refer photometry in different magnitude systems to the same flux scale, for example providing simultaneously homogeneous JKC, SDSS, PS1, and HST photometry for the same set of stars. In perspective, this should be the essential contribution of the *Gaia* XPSP: providing an absolute photometric reference for optical photometry, while the astrophysical information of the observed sources can, in principle, be optimally extracted from the entire XP spectra.

There are sound arguments for believing that the performance we present here can significantly improve in future *Gaia* data releases (see also De Angeli et al. 2023; Montegriffo et al. 2023). The accumulation of many additional epoch spectra will provide mean XP spectra with higher S/N and consequently more precise XPSP. The release of XP spectra for fainter stars will significantly enhance the photometric depth that can be reached, well beyond the current $G < 17.65$ limit. New, improved releases of the SPSS will provide a more robust basis for a more accurate flux scale of XP ECS and a better calibration of the instrument model, a vital ingredient of the chain leading to XPSP. There are ideas to improve the calibration of the instrument model by other means; for example by a better calibration of the LSF, of the wavelength scale, and so on, to be implemented in the next cycle of data reduction. The internal calibration of mean XP spectra will improve in future releases. For example, there is currently a lot of work being done to improve the algorithm for sky subtraction, which could imply substantial mitigation of the hockey-stick effect. In general, each *Gaia* data release improves upon the entire process of spectro-photometry, as we gain experience in the instruments and the ways to calibrate for even the smallest of effects, and new pieces of the calibration are activated.

If significant mitigation of residual systematic errors were indeed to be achieved, this would greatly extend the contribution of the *Gaia* mission to optical photometry.

Acknowledgements. This work presents results from the European Space Agency (ESA) space mission *Gaia*. *Gaia* data are being processed by the *Gaia* Data Processing and Analysis Consortium (DPAC). Funding for the DPAC is provided by national institutions, in particular the institutions participating in the *Gaia* MultiLateral Agreement (MLA). The *Gaia* mission website is `https://www.cosmos.esa.int/gaia`. The *Gaia* archive website is `https://archives.esac.esa.int/gaia`. The full acknowledgements are available in Appendix A.

Note added in proof. Due to a bug in GaiaXPy the synthetic photometry for the standardized PS1 y band photometry published in the GSPC (contained in the fields `y_ps1_flux`, `y_ps1_flux_error` and `y_ps1_mag`) has been generated without applying the correction for the hockey-stick effect. The *Gaia* Archive table `gaiadr3.synthetic_photometry_gspc` will not be fixed. However, correct synthetic photometry in the standardised PS1 system can be generated using GaiaXPy (with version 1.2.4 or later) on spectra extracted from the archive. Prior to version 1.2.4, the GaiaXPy bug gave the same error for all the PS1 passbands, but y was the only PS1 flux/magnitude included in GSPC. It has also been discovered that the units of the SDSS and PS1 flux and flux error fields in the GSPC are wrong and should have Hz^{-1} instead of nm^{-1}. Only the units are wrong: the data contained in the table is correct (except for the issue described above regarding y_{PS1}).

References

Aguado, D. S., Youakim, K., González Hernández, J. I., et al. 2019, MNRAS, 490, 2241
Ahn, C. P., Alexandroff, R., Allende Prieto, C., et al. 2012, ApJS, 203, 21
Ahumada, R., Allende Prieto, C., Almeida, A., et al. 2020, ApJS, 249, 3
Allard, F., Homeier, D., Freytag, B., Schaffenberger, W., & Rajpurohit, A. S. 2013, Mem. Soc. Astron. It. Suppl., 24, 128
Alonso, A., Arribas, S., & Martínez-Roger, C. 1999, A&AS, 140, 261
Altavilla, G., Marinoni, S., Pancino, E., et al. 2021, MNRAS, 501, 2848
Andrae, R., Fouesneau, M., Sordo, R., et al. 2023, A&A, 674, A27 (*Gaia* DR3 SI)
Anthony-Twarog, B. J., & Twarog, B. A. 2000, AJ, 120, 3111
Astropy Collaboration (Price-Whelan, A., et al.) 2018, AJ, 156, 123
Bailer-Jones, C. A. L., Rybizki, J., Fouesneau, M., Demleitner, M., & Andrae, R. 2021, AJ, 161, 147
Bastian, N., & Lardo, C. 2018, ARA&A, 56, 83
Bedin, L. R., Salaris, M., Anderson, J., et al. 2019, MNRAS, 488, 3857
Beers, T. C., & Christlieb, N. 2005, ARA&A, 43, 531
Beers, T. C., Preston, G. W., & Shectman, S. A. 1985, AJ, 90, 2089
Benitez, N., Dupke, R., Moles, M., et al. 2014, ArXiv e-prints [arXiv:1403.5237]
Bessell, M. S. 2005, ARA&A, 43, 293
Bessell, M. S. 2011, PASP, 123, 1442
Bessell, M., & Murphy, S. 2012, PASP, 124, 140
Birko, D., Zwitter, T., Grebel, E. K., et al. 2019, AJ, 158, 155
Blanton, M. R., Bershady, M. A., Abolfathi, B., et al. 2017, AJ, 154, 28
Boch, T., & Fernique, P. 2014, in Astronomical Data Analysis Software and Systems XXIII, eds. N. Manset, & P. Forshay, ASP Conf. Ser., 485, 277
Bohlin, R. C. 2014, AJ, 147, 127
Bonnarel, F., Fernique, P., Bienaymé, O., et al. 2000, A&AS, 143, 33
Bonoli, S., Marín-Franch, A., Varela, J., et al. 2021, A&A, 653, A31
Bossini, D., Vallenari, A., Bragaglia, A., et al. 2019, A&A, 623, A108
Bragaglia, A., Carretta, E., Gratton, R. G., et al. 2001, AJ, 121, 327
Bragaglia, A., Sneden, C., Carretta, E., et al. 2014, ApJ, 796, 68
Bressan, A., Marigo, P., Girardi, L., et al. 2012, MNRAS, 427, 127
Buder, S., Sharma, S., Kos, J., et al. 2021, MNRAS, 506, 150
Calamida, A., Bono, G., Stetson, P. B., et al. 2007, ApJ, 670, 400
Cantat-Gaudin, T., Anders, F., Castro-Ginard, A., et al. 2020, A&A, 640, A1
Cardelli, J. A., Clayton, G. C., & Mathis, J. S. 1989, ApJ, 345, 245

Carrasco, J. M., Weiler, M., Jordi, C., et al. 2021, A&A, 652, A86
Carretta, E., Bragaglia, A., Gratton, R. G., & Tosi, M. 2004, A&A, 422, 951
Carretta, E., Bragaglia, A., Gratton, R., D'Orazi, V., & Lucatello, S. 2009, A&A, 508, 695
Carretta, E., Bragaglia, A., Gratton, R., D'Orazi, V., & Lucatello, S. 2011, A&A, 535, A121
Cenarro, A. J., Moles, M., Marín-Franch, A., et al. 2014, in Observatory Operations: Strategies, Processes, and Systems V, eds. A. B. Peck, C. R. Benn, & R. L. Seaman, SPIE Conf. Ser., 9149, 91491I
Cenarro, A. J., Moles, M., Cristóbal-Hornillos, D., et al. 2019, A&A, 622, A176
Chambers, K. C., Magnier, E. A., Metcalfe, N., et al. 2016, ArXiv e-prints [arXiv:1612.05560]
Chen, Y., Girardi, L., Fu, X., et al. 2019, A&A, 632, A105
Chen, X., Wang, S., Deng, L., et al. 2020, ApJS, 249, 18
Christlieb, N., Wisotzki, L., & Graßhoff, G. 2002, A&A, 391, 397
Clem, J. L., & Landolt, A. U. 2013, AJ, 146, 88
Clem, J. L., & Landolt, A. U. 2016, AJ, 152, 91
Cousins, A. W. J. 1973, Mem. R. Astron. Soc., 77, 223
Cousins, A. W. J. 1983, S. Afr. Astron. Obs. Circ., 7, 47
Cousins, A. W. J. 1984, S. Afr. Astron. Obs. Circ., 8, 59
Crawford, D. L., & Barnes, J. V. 1970, AJ, 75, 978
Creevey, O., Sordo, R., Pailler, F., et al. 2023, A&A, 674, A26 (*Gaia* DR3 SI)
Cui, X.-Q., Zhao, Y.-H., Chu, Y.-Q., et al. 2012, Res. Astron. Astrophys., 12, 1197
De Angeli, F., Weiler, M., Montegriffo, P., et al. 2023, A&A, 674, A2 (*Gaia* DR3 SI)
Deleuil, M., Aigrain, S., Moutou, C., et al. 2018, A&A, 619, A97
Doi, M., Tanaka, M., Fukugita, M., et al. 2010, AJ, 139, 1628
Drew, J. E., Greimel, R., Irwin, M. J., et al. 2005, MNRAS, 362, 753
Drew, J. E., Gonzalez-Solares, E., Greimel, R., et al. 2014, MNRAS, 440, 2036
Eisenstein, D. J., Weinberg, D. H., Agol, E., et al. 2011, AJ, 142, 72
Evans, D. W., Riello, M., De Angeli, F., et al. 2018, A&A, 616, A4
Fabricius, C., Høg, E., Makarov, V. V., et al. 2002, A&A, 384, 180
Flewelling, H. A., Magnier, E. A., Chambers, K. C., et al. 2020, ApJS, 251, 7
Fouesneau, M., Frémat, Y., Andrae, R., et al. 2023, A&A, 674, A28 (*Gaia* DR3 SI)
Frank, M. J., Koch, A., Feltzing, S., et al. 2015, A&A, 581, A72
Fritzewski, D. J., Barnes, S. A., James, D. J., et al. 2019, A&A, 622, A110
Fukugita, M., Ichikawa, T., Gunn, J. E., et al. 1996, AJ, 111, 1748
Gaia Collaboration (Prusti, T., et al.) 2016, A&A, 595, A1
Gaia Collaboration (Brown, A. G. A., et al.) 2018a, A&A, 616, A1
Gaia Collaboration (Babusiaux, C., et al.) 2018b, A&A, 616, A10
Gaia Collaboration (Eyer, L., et al.) 2019, A&A, 623, A110
Gaia Collaboration (Smart, R. L., et al.) 2021a, A&A, 649, A6
Gaia Collaboration (Brown, A. G. A., et al.) 2021b, A&A, 649, A1
Gaia Collaboration (Vallenari, A., et al.) 2023a, A&A, 674, A1 (*Gaia* DR3 SI)
Gaia Collaboration (Bailer-Jones, C., et al.) 2023b, A&A, 674, A41 (*Gaia* DR3 SI)
Gaia Collaboration (Recio-Blanco, A., et al.) 2023c, A&A, 674, A38 (*Gaia* DR3 SI)
Gavel, A., Andrae, R., Fouesneau, M., Korn, A. J., & Sordo, R. 2021, A&A, 656, A93
Gentile Fusillo, N. P., Tremblay, P.-E., Gänsicke, B. T., et al. 2019, MNRAS, 482, 4570
Gentile Fusillo, N. P., Tremblay, P. E., Cukanovaite, E., et al. 2021, MNRAS, 508, 3877
Gratton, R., Bragaglia, A., Carretta, E., et al. 2019, A&ARv, 27, 8
Greif, T. H. 2015, Comput. Astrophys. Cosmol., 2, 3
Grundahl, F., Briley, M., Nissen, P. E., & Feltzing, S. 2002, A&A, 385, L14
Harris, W. E. 1996, AJ, 112, 1487
Harris, C. R., Millman, K. J., van der Walt, S. J., et al. 2020, Nature, 585, 357
Hauck, B., & Mermilliod, M. 1998, A&AS, 129, 431
Heap, S. R., & Lindler, D. 2016, in The Science of Calibration, eds. S. Deustua, S. Allam, D. Tucker, & J. A. Smith, ASP Conf. Ser., 503, 211
Høg, E., Fabricius, C., Makarov, V. V., et al. 2000, A&A, 355, L27
Huang, B., & Yuan, H. 2022, ApJS, 259, 26
Huang, Y., Yuan, H., Li, C., et al. 2021, ApJ, 907, 68
Huang, Y., Beers, T. C., Wolf, C., et al. 2022, ApJ, 925, 164
Hunter, J. D. 2007, Comput. Sci. Eng., 9, 90
Ivezić, Ž., Smith, J. A., Miknaitis, G., et al. 2007, AJ, 134, 973
Jao, W.-C., & Feiden, G. A. 2020, AJ, 160, 102
Jao, W.-C., Henry, T. J., Gies, D. R., & Hambly, N. C. 2018, ApJ, 861, L11
Jayasinghe, T., Kochanek, C. S., Stanek, K. Z., et al. 2018, MNRAS, 477, 3145
Jayasinghe, T., Stanek, K. Z., Kochanek, C. S., et al. 2019a, MNRAS, 485, 961
Jayasinghe, T., Stanek, K. Z., Kochanek, C. S., et al. 2019b, MNRAS, 486, 1907
Johnson, H. L. 1963, in Basic Astronomical Data: Stars and Stellar Systems, ed. K. A. Strand (Chicago: University of Chicago Press), 204
Johnson, H. L., & Morgan, W. W. 1953, ApJ, 117, 313
Jordi, C., Høg, E., Brown, A. G. A., et al. 2006, MNRAS, 367, 290
Karlsson, T., Bromm, V., & Bland-Hawthorn, J. 2013, Rev. Mod. Phys., 85, 809
Kirk, B., Conroy, K., Prša, A., et al. 2016, AJ, 151, 68
Kleinman, S. J., Kepler, S. O., Koester, D., et al. 2013, ApJS, 204, 5
Kounkel, M., Covey, K. R., Stassun, K. G., et al. 2021, AJ, 162, 184
Kron, G. E., White, H. S., & Gascoigne, S. C. B. 1953, ApJ, 118, 502
Landolt, A. U. 1992, AJ, 104, 340
Landolt, A. U. 2007, AJ, 133, 2502
Landolt, A. U. 2009, AJ, 137, 4186
Landolt, A. U. 2011, in Astronomical Photometry: Past, Present, and Future, eds. E. F. F. Milone, & C. Sterken, Astrophys. Space Sci. Lib., 373, 109
Landolt, A. U. 2013, AJ, 146, 131
Landolt, A. U., & Uomoto, A. K. 2007, AJ, 133, 768
Lardo, C., Bellazzini, M., Pancino, E., et al. 2011, A&A, 525, A114
Lardo, C., Pancino, E., Mucciarelli, A., & Milone, A. P. 2012, A&A, 548, A107
Lardo, C., Pancino, E., Mucciarelli, A., et al. 2013, MNRAS, 433, 1941
Lee, J.-W. 2019, ApJ, 872, 41
Lindegren, L., Klioner, S. A., Hernández, J., et al. 2021, A&A, 649, A2
López-Sanjuan, C., Varela, J., Cristóbal-Hornillos, D., et al. 2019, A&A, 631, A119
López-Sanjuan, C., Yuan, H., Vázquez Ramió, H., et al. 2021, A&A, 654, A61
López-Sanjuan, C., Tremblay, P. E., Ederoclite, A., et al. 2022, A&A, 658, A79
Macchetto, D. F. 2010, in The Impact of HST on European Astronomy, Astrophys. Space Sci. Proc., 15
Magnier, E. A., Schlafly, E. F., Finkbeiner, D. P., et al. 2020a, ApJS, 251, 6
Magnier, E. A., Chambers, K. C., Flewelling, H. A., et al. 2020b, ApJS, 251, 3
Magnier, E. A., Sweeney, W. E., Chambers, K. C., et al. 2020c, ApJS, 251, 5
Manfroid, J. 1992, A&A, 260, 517
Massari, D., Lapenna, E., Bragaglia, A., et al. 2016, MNRAS, 458, 4162
Merle, T., Van Eck, S., Jorissen, A., et al. 2017, A&A, 608, A95
Milone, E. F., & Sterken, C. 2011, in Astronomical Photometry: Past, Present, and Future (Berlin: Springer), Astrophys. Space Sci. Lib., 373
Milone, A. P., Piotto, G., Bedin, L. R., et al. 2012, ApJ, 744, 58
Milone, A. P., Marino, A. F., Piotto, G., et al. 2013, ApJ, 767, 120
Milone, A. P., Marino, A. F., Piotto, G., et al. 2015, MNRAS, 447, 927
Monelli, M., Milone, A. P., Stetson, P. B., et al. 2013, MNRAS, 431, 2126
Monguió, M., Figueras, F., & Grosbøl, P. 2013, A&A, 549, A78
Monguió, M., Greimel, R., Drew, J. E., et al. 2020, A&A, 638, A18
Montegriffo, P., De Angeli, F., Andrae, R., et al. 2023, A&A, 674, A3 (*Gaia* DR3 SI)
Mowlavi, N., Rimoldini, L., Evans, D. W., et al. 2021, A&A, 648, A44
Nardiello, D., Libralato, M., Piotto, G., et al. 2018, MNRAS, 481, 3382
Ochsenbein, F., Bauer, P., & Marcout, J. 2000, A&AS, 143, 23
Onken, C. A., Wolf, C., Bessell, M. S., et al. 2019, PASA, 36, e033
Pancino, E., Ferraro, F. R., Bellazzini, M., Piotto, G., & Zoccali, M. 2000, ApJ, 534, L83
Pancino, E., Rejkuba, M., Zoccali, M., & Carrera, R. 2010, A&A, 524, A44
Pancino, E., Bellazzini, M., Giuffrida, G., & Marinoni, S. 2017, MNRAS, 467, 412
Pancino, E., Sanna, N., Altavilla, G., et al. 2021, MNRAS, 503, 3660
Pancino, E., Marrese, P. M., Marinoni, S., et al. 2022, A&A, 664, A109
Pel, J. W., & Lub, J. 2007, in The Future of Photometric, Spectrophotometric and Polarimetric Standardization, ed. C. Sterken, ASP Conf. Ser., 364, 63
Pérez, F., & Granger, B. E. 2007, Comput. Sci. Eng., 9, 21
Piatti, A. E., Pietrzyński, G., Narloch, W., Górski, M., & Graczyk, D. 2019, MNRAS, 483, 4766
Piotto, G., Bedin, L. R., Anderson, J., et al. 2007, ApJ, 661, L53
Price-Whelan, A. M., Hogg, D. W., Rix, H.-W., et al. 2020, ApJ, 895, 2
Qian, S.-B., Shi, X.-D., Zhu, L.-Y., et al. 2019, Res. Astron. Astrophys., 19, 064
R Core Team 2013, R: A Language and Environment for Statistical Computing, R Foundation for Statistical Computing, Vienna, Austria
Richter, P., Hilker, M., & Richtler, T. 1999, A&A, 350, 476
Riello, M., De Angeli, F., Evans, D. W., et al. 2021, A&A, 649, A3
Rodrigo, C., & Solano, E. 2020, XIV.0 Scientific Meeting (virtual) of the Spanish Astronomical Society, 182
Rodríguez-Flores, E. R., Corradi, R. L. M., Mampaso, A., et al. 2014, A&A, 567, A49
Rufener, F. G. 1971, A&AS, 3, 181
Savino, A., Massari, D., Bragaglia, A., Dalessandro, E., & Tolstoy, E. 2018, MNRAS, 474, 4438
Sbordone, L., Salaris, M., Weiss, A., & Cassisi, S. 2011, A&A, 534, A9
Scaringi, S., Knigge, C., Drew, J., et al. 2018, MNRAS, 481, 3357
Shappee, B. J., Prieto, J. L., Grupe, D., et al. 2014, ApJ, 788, 48
Sirianni, M., Jee, M. J., Benítez, N., et al. 2005, PASP, 117, 1049
Starkenburg, E., Martin, N., Youakim, K., et al. 2017, MNRAS, 471, 2587
Sterken, C. 2007a, ASP Conf. Ser., 364, 613

Sterken, C. 2007b, ASP Conf. Ser., 364, 3
Sterken, C., Milone, E. F., & Young, A. T. 2011, in Astronomical Photometry: Past, Present, and Future, eds. E. F. F. Milone, & C. Sterken, Astrophys. Space Sci. Lib., 373, 1
Stetson, P. B., Pancino, E., Zocchi, A., Sanna, N., & Monelli, M. 2019, MNRAS, 485, 3042
Strömgren, B. 1956, Vistas Astron., 2, 1336
Stubbs, C. W., & Tonry, J. L. 2006, ApJ, 646, 1436
Taylor, M. B. 2005, in Astronomical Data Analysis Software and Systems XIV, eds. P. Shopbell, M. Britton, & R. Ebert, ASP Conf. Ser., 347, 29
Taylor, B. J. 2006a, AJ, 132, 2453
Taylor, M. B. 2006b, in Astronomical Data Analysis Software and Systems XV, eds. C. Gabriel, C. Arviset, D. Ponz, & S. Enrique, ASP Conf. Ser., 351, 666
Thanjavur, K., Ivezić, Ž., Allam, S. S., et al. 2021, MNRAS, 505, 5941
Tian, H.-J., El-Badry, K., Rix, H.-W., & Gould, A. 2020, ApJS, 246, 4
Traven, G., Feltzing, S., Merle, T., et al. 2020, A&A, 638, A145
Tsantaki, M., Pancino, E., Marrese, P., et al. 2022, A&A, 659, A95
van der Maaten, L., & Hinton, G. 2008, J. Mach. Learn. Res., 9, 2579
van Leeuwen, F. 2007, A&A, 474, 653
van Leeuwen, F., Evans, D. W., Grenon, M., et al. 1997, A&A, 323, L61
VandenBerg, D. A., Brogaard, K., Leaman, R., & Casagrande, L. 2013, ApJ, 775, 134
Vasiliev, E., & Baumgardt, H. 2021, MNRAS, 505, 5978
Waters, C. Z., Magnier, E. A., Price, P. A., et al. 2020, ApJS, 251, 4
Wenger, M., Ochsenbein, F., Egret, D., et al. 2000, A&AS, 143, 9
Wolf, C., Onken, C. A., Luvaul, L. C., et al. 2018, PASA, 35, e010
Xiao, K., & Yuan, H. 2022, AJ, 163, 4
Yanny, B., Rockosi, C., Newberg, H. J., et al. 2009, AJ, 137, 4377
Yong, D., Grundahl, F., Johnson, J. A., & Asplund, M. 2008, ApJ, 684, 1159
York, D. G., Adelman, J., Anderson, J. E., Jr., et al. 2000, AJ, 120, 1579
Young, A. T. 1992a, in Automated Telescopes for Photometry and Imaging, eds. S. J. Adelman, J. Dukes, J. Robert, & C. J. Adelman, ASP Conf. Ser., 28, 73
Young, A. T. 1992b, A&A, 257, 366
Young, A. T. 1994a, A&A, 288, 683
Young, A. T. 1994b, in The Impact of Long-Term Monitoring on Variable Star Research: Astrophysics, eds. C. Sterken, & M. de Groot, NATO Adv. Study Inst. (ASI) Ser. C, 436, 421
Zhang, R., Lucatello, S., Bragaglia, A., et al. 2021, A&A, 654, A77

[1] INAF – Osservatorio di Astrofisica e Scienza dello Spazio di Bologna, Via Piero Gobetti 93/3, 40129 Bologna, Italy
[2] Institute of Astronomy, University of Cambridge, Madingley Road, Cambridge CB3 0HA, UK
[3] Max Planck Institute for Astronomy, Königstuhl 17, 69117 Heidelberg, Germany
[4] School of Physics and Astronomy/Space Park Leicester, University of Leicester, University Road, Leicester LE1 7RH, UK
[5] Instituto de Astrofísica e Ciências do Espaço, Universidade do Porto, CAUP, Rua das Estrelas, 4150-762 Porto, Portugal
[6] Institut de Ciències del Cosmos (ICCUB), Universitat de Barcelona (IEEC-UB), Martí i Franquès 1, 08028 Barcelona, Spain
[7] Institut d'Astrophysique et de Géophysique, Université de Liège, 19c, Allée du 6 Août, 4000 Liège, Belgium
[8] Royal Observatory of Belgium, Ringlaan 3, 1180 Brussels, Belgium
[9] CIGUS CITIC – Department of Computer Science and Information Technologies, University of A Coruña, Campus de Elviña s/n, A Coruña 15071, Spain
[10] CIGUS CITIC, Department of Nautical Sciences and Marine Engineering, University of A Coruña, Paseo de Ronda 51, 15071 A Coruña, Spain
[11] Ruđer Bošković Institute, Bijenička cesta 54, 10000 Zagreb, Croatia
[12] INAF – Osservatorio Astrofisico di Arcetri, Largo Enrico Fermi 5, 50125 Firenze, Italy
[13] Space Science Data Center – ASI, Via del Politecnico SNC, 00133 Roma, Italy
[14] INAF – Osservatorio astronomico di Padova, Vicolo Osservatorio 5, 35122 Padova, Italy
[15] Leiden Observatory, Leiden University, Niels Bohrweg 2, 2333 CA Leiden, The Netherlands
[16] European Space Agency (ESA), European Space Research and Technology Centre (ESTEC), Keplerlaan 1, 2201 AZ Noordwijk, The Netherlands
[17] GEPI, Observatoire de Paris, Université PSL, CNRS, 5 Place Jules Janssen, 92190 Meudon, France
[18] Univ. Grenoble Alpes, CNRS, IPAG, 38000 Grenoble, France
[19] Astronomisches Rechen-Institut, Zentrum für Astronomie der Universität Heidelberg, Mönchhofstr. 12-14, 69120 Heidelberg, Germany
[20] Université Côte d'Azur, Observatoire de la Côte d'Azur, CNRS, Laboratoire Lagrange, Bd de l'Observatoire, CS 34229, 06304 Nice Cedex 4, France
[21] Laboratoire d'Astrophysique de Bordeaux, Univ. Bordeaux, CNRS, B18N, Allée Geoffroy Saint-Hilaire, 33615 Pessac, France
[22] Department of Astronomy, University of Geneva, Chemin Pegasi 51, 1290 Versoix, Switzerland
[23] European Space Agency (ESA), European Space Astronomy Centre (ESAC), Camino Bajo del Castillo, s/n, Urbanizacion Villafranca del Castillo, Villanueva de la Cañada 28692, Madrid, Spain
[24] Aurora Technology for European Space Agency (ESA), Camino Bajo del Castillo, s/n, Urbanizacion Villafranca del Castillo, Villanueva de la Cañada 28692, Madrid, Spain
[25] Lohrmann Observatory, Technische Universität Dresden, Mommsenstraße 13, 01062 Dresden, Germany
[26] Lund Observatory, Department of Astronomy and Theoretical Physics, Lund University, Box 43, 22100 Lund, Sweden
[27] CNES Centre Spatial de Toulouse, 18 Avenue Edouard Belin, 31401 Toulouse Cedex 9, France
[28] Institut d'Astronomie et d'Astrophysique, Université Libre de Bruxelles CP 226, Boulevard du Triomphe, 1050 Brussels, Belgium
[29] F.R.S.-FNRS, Rue d'Egmont 5, 1000 Brussels, Belgium
[30] INAF – Osservatorio Astrofisico di Torino, Via Osservatorio 20, 10025 Pino Torinese, TO, Italy
[31] European Space Agency (ESA), Noordwijk, The Netherlands
[32] University of Turin, Department of Physics, Via Pietro Giuria 1, 10125 Torino, Italy
[33] DAPCOM for Institut de Ciències del Cosmos (ICCUB), Universitat de Barcelona (IEEC-UB), Martí i Franquès 1, 08028 Barcelona, Spain
[34] Observational Astrophysics, Division of Astronomy and Space Physics, Department of Physics and Astronomy, Uppsala University, Box 516, 751 20 Uppsala, Sweden
[35] ALTEC S.p.a, Corso Marche 79, 10146 Torino, Italy
[36] Sednai Sàrl, Geneva, Switzerland
[37] Department of Astronomy, University of Geneva, Chemin d'Ecogia 16, 1290 Versoix, Switzerland
[38] Mullard Space Science Laboratory, University College London, Holmbury St Mary, Dorking, Surrey RH5 6NT, UK
[39] Gaia DPAC Project Office, ESAC, Camino Bajo del Castillo, s/n, Urbanizacion Villafranca del Castillo, Villanueva de la Cañada 28692, Madrid, Spain
[40] Telespazio UK S.L. for European Space Agency (ESA), Camino Bajo del Castillo, s/n, Urbanizacion Villafranca del Castillo, Villanueva de la Cañada 28692, Madrid, Spain
[41] SYRTE, Observatoire de Paris, Université PSL, CNRS, Sorbonne Université, LNE, 61 Avenue de l'Observatoire, 75014 Paris, France
[42] National Observatory of Athens, I. Metaxa and Vas. Pavlou, Palaia Penteli, 15236 Athens, Greece
[43] IMCCE, Observatoire de Paris, Université PSL, CNRS, Sorbonne Université, Univ. Lille, 77 Av. Denfert-Rochereau, 75014 Paris, France
[44] Serco Gestión de Negocios for European Space Agency (ESA), Camino Bajo del Castillo, s/n, Urbanizacion Villafranca del Castillo, Villanueva de la Cañada 28692, Madrid, Spain
[45] CRAAG – Centre de Recherche en Astronomie, Astrophysique et Géophysique, Route de l'Observatoire Bp 63 Bouzareah, 16340 Algiers, Algeria

[46] Institute for Astronomy, University of Edinburgh, Royal Observatory, Blackford Hill, Edinburgh EH9 3HJ, UK
[47] RHEA for European Space Agency (ESA), Camino Bajo del Castillo, s/n, Urbanizacion Villafranca del Castillo, Villanueva de la Cañada 28692, Madrid, Spain
[48] ATG Europe for European Space Agency (ESA), Camino Bajo del Castillo, s/n, Urbanizacion Villafranca del Castillo, Villanueva de la Cañada 28692, Madrid, Spain
[49] Université de Strasbourg, CNRS, Observatoire Astronomique de Strasbourg, UMR 7550, 11 Rue de l'Université, 67000 Strasbourg, France
[50] Kavli Institute for Cosmology Cambridge, Institute of Astronomy, Madingley Road, Cambridge CB3 0HA, UK
[51] Leibniz Institute for Astrophysics Potsdam (AIP), An der Sternwarte 16, 14482 Potsdam, Germany
[52] CENTRA, Faculdade de Ciências, Universidade de Lisboa, Edif. C8, Campo Grande, 1749-016 Lisboa, Portugal
[53] Department of Informatics, Donald Bren School of Information and Computer Sciences, University of California, Irvine, 5226 Donald Bren Hall, 92697-3440, CA Irvine, USA
[54] INAF – Osservatorio Astrofisico di Catania, Via S. Sofia 78, 95123 Catania, Italy
[55] Dipartimento di Fisica e Astronomia "Ettore Majorana", Università di Catania, Via S. Sofia 64, 95123 Catania, Italy
[56] INAF – Osservatorio Astronomico di Roma, Via Frascati 33, 00078 Monte Porzio Catone, Roma, Italy
[57] Department of Physics, University of Helsinki, PO Box 64, 00014 Helsinki, Finland
[58] Finnish Geospatial Research Institute FGI, Geodeetinrinne 2, 02430 Masala, Finland
[59] Institut UTINAM CNRS UMR6213, Université Bourgogne Franche-Comté, OSU THETA Franche-Comté Bourgogne, Observatoire de Besançon, BP 1615, 25010 Besançon Cedex, France
[60] HE Space Operations BV for European Space Agency (ESA), Keplerlaan 1, 2201 AZ Noordwijk, The Netherlands
[61] Dpto. de Inteligencia Artificial, UNED, c/ Juan del Rosal 16, 28040 Madrid, Spain
[62] Konkoly Observatory, Research Centre for Astronomy and Earth Sciences, Eötvös Loránd Research Network (ELKH), MTA Centre of Excellence, Konkoly Thege Miklós út 15-17, 1121 Budapest, Hungary
[63] ELTE Eötvös Loránd University, Institute of Physics, 1117, Pázmány Péter sétány 1A, Budapest, Hungary
[64] Instituut voor Sterrenkunde, KU Leuven, Celestijnenlaan 200D, 3001 Leuven, Belgium
[65] Department of Astrophysics/IMAPP, Radboud University, PO Box 9010, 6500 GL Nijmegen, The Netherlands
[66] University of Vienna, Department of Astrophysics, Türkenschanzstraße 17, 1180 Vienna, Austria
[67] Institute of Physics, Laboratory of Astrophysics, Ecole Polytechnique Fédérale de Lausanne (EPFL), Observatoire de Sauverny, 1290 Versoix, Switzerland
[68] Kapteyn Astronomical Institute, University of Groningen, Landleven 12, 9747 AD Groningen, The Netherlands
[69] Thales Services for CNES Centre Spatial de Toulouse, 18 Avenue Edouard Belin, 31401 Toulouse Cedex 9, France
[70] Depto. Estadística e Investigación Operativa. Universidad de Cádiz, Avda. República Saharaui s/n, 11510 Puerto Real, Cádiz, Spain
[71] Center for Research and Exploration in Space Science and Technology, University of Maryland Baltimore County, 1000 Hilltop Circle, Baltimore, MD, USA
[72] GSFC – Goddard Space Flight Center, Code 698, 8800 Greenbelt Rd, 20771, MD Greenbelt, USA
[73] EURIX S.r.l., Corso Vittorio Emanuele II 61, 10128 Torino, Italy
[74] Porter School of the Environment and Earth Sciences, Tel Aviv University, Tel Aviv 6997801, Israel
[75] Harvard-Smithsonian Center for Astrophysics, 60 Garden St., MS 15, Cambridge, MA 02138, USA
[76] HE Space Operations BV for European Space Agency (ESA), Camino Bajo del Castillo, s/n, Urbanizacion Villafranca del Castillo, Villanueva de la Cañada 28692, Madrid, Spain
[77] LFCA/DAS,Universidad de Chile,CNRS, Casilla 36-D, Santiago, Chile
[78] SISSA – Scuola Internazionale Superiore di Studi Avanzati, Via Bonomea 265, 34136 Trieste, Italy
[79] Telespazio for CNES Centre Spatial de Toulouse, 18 Avenue Edouard Belin, 31401 Toulouse Cedex 9, France
[80] University of Turin, Department of Computer Sciences, Corso Svizzera 185, 10149 Torino, Italy
[81] Dpto. de Matemática Aplicada y Ciencias de la Computación, Univ. de Cantabria, ETS Ingenieros de Caminos, Canales y Puertos, Avda. de los Castros s/n, 39005 Santander, Spain
[82] Centro de Astronomía – CITEVA, Universidad de Antofagasta, Avenida Angamos 601, Antofagasta 1270300, Chile
[83] DLR Gesellschaft für Raumfahrtanwendungen (GfR), mbH Münchener Straße 20, 82234, Weßling, Germany
[84] Centre for Astrophysics Research, University of Hertfordshire, College Lane AL10 9AB, Hatfield, UK
[85] University of Turin, Mathematical Department "G. Peano", Via Carlo Alberto 10, 10123 Torino, Italy
[86] INAF – Osservatorio Astronomico d'Abruzzo, Via Mentore Maggini, 64100 Teramo, Italy
[87] Instituto de Astronomia, Geofisica e Ciências Atmosféricas, Universidade de São Paulo, Rua do Matão, 1226, Cidade Universitaria, 05508-900 São Paulo, SP, Brazil
[88] APAVE SUDEUROPE SAS for CNES Centre Spatial de Toulouse, 18 Avenue Edouard Belin, 31401 Toulouse Cedex 9, France
[89] Mésocentre de calcul de Franche-Comté, Université de Franche-Comté, 16 Route de Gray, 25030 Besançon Cedex, France
[90] ATOS for CNES Centre Spatial de Toulouse, 18 Avenue Edouard Belin, 31401 Toulouse Cedex 9, France
[91] School of Physics and Astronomy, Tel Aviv University, Tel Aviv 6997801, Israel
[92] Astrophysics Research Centre, School of Mathematics and Physics, Queen's University Belfast, Belfast BT7 1NN, UK
[93] Centre de Données Astronomique de Strasbourg, Strasbourg, France
[94] Institute for Computational Cosmology, Department of Physics, Durham University, Durham DH1 3LE, UK
[95] European Southern Observatory, Karl-Schwarzschild-Str. 2, 85748 Garching, Germany
[96] Max-Planck-Institut für Astrophysik, Karl-Schwarzschild-Straße 1, 85748 Garching, Germany
[97] Data Science and Big Data Lab., Pablo de Olavide University, 41013 Seville, Spain
[98] Barcelona Supercomputing Center (BSC), Plaça Eusebi Güell 1-3, 08034 Barcelona, Spain
[99] ETSE Telecomunicación, Universidade de Vigo, Campus Lagoas-Marcosende, 36310 Vigo, Galicia, Spain
[100] Asteroid Engineering Laboratory, Space Systems, Luleå University of Technology, Box 848, 981 28 Kiruna, Sweden
[101] Vera C Rubin Observatory, 950 N. Cherry Avenue, Tucson, AZ 85719, USA
[102] Department of Astrophysics, Astronomy and Mechanics, National and Kapodistrian University of Athens, Panepistimiopolis, Zografos 15783, Athens, Greece
[103] TRUMPF Photonic Components GmbH, Lise-Meitner-Straße 13, 89081 Ulm, Germany
[104] IAC – Instituto de Astrofisica de Canarias, Via Láctea s/n, 38200 La Laguna S.C., Tenerife, Spain
[105] Department of Astrophysics, University of La Laguna, Via Láctea s/n, 38200 La Laguna S.C., Tenerife, Spain
[106] Faculty of Aerospace Engineering, Delft University of Technology, Kluyverweg 1, 2629 HS Delft, The Netherlands
[107] Radagast Solutions, Simon Vestdijkpad 24, 2321 WD Leiden, The Netherlands

[108] Laboratoire Univers et Particules de Montpellier, CNRS Université Montpellier, Place Eugène Bataillon, CC72, 34095 Montpellier Cedex 05, France
[109] Université de Caen Normandie, Côte de Nacre, Boulevard Maréchal Juin, 14032 Caen, France
[110] LESIA, Observatoire de Paris, Université PSL, CNRS, Sorbonne Université, Université de Paris, 5 Place Jules Janssen, 92190 Meudon, France
[111] SRON Netherlands Institute for Space Research, Niels Bohrweg 4, 2333 CA Leiden, The Netherlands
[112] Astronomical Observatory, University of Warsaw, Al. Ujazdowskie 4, 00-478 Warszawa, Poland
[113] Scalian for CNES Centre Spatial de Toulouse, 18 Avenue Edouard Belin, 31401 Toulouse Cedex 9, France
[114] Université Rennes, CNRS, IPR (Institut de Physique de Rennes), UMR 6251, 35000 Rennes, France
[115] INAF – Osservatorio Astronomico di Capodimonte, Via Moiariello 16, 80131 Napoli, Italy
[116] Shanghai Astronomical Observatory, Chinese Academy of Sciences, 80 Nandan Road, Shanghai 200030, PR China
[117] University of Chinese Academy of Sciences, No. 19(A) Yuquan Road, Shijingshan District, Beijing 100049, PR China
[118] Niels Bohr Institute, University of Copenhagen, Juliane Maries Vej 30, 2100 Copenhagen Ø, Denmark
[119] DXC Technology, Retortvej 8, 2500 Valby, Denmark
[120] Las Cumbres Observatory, 6740 Cortona Drive Suite 102, Goleta, CA 93117, USA
[121] Astrophysics Research Institute, Liverpool John Moores University, 146 Brownlow Hill, Liverpool L3 5RF, UK
[122] IPAC, Mail Code 100-22, California Institute of Technology, 1200 E. California Blvd., Pasadena, CA 91125, USA
[123] IRAP, Université de Toulouse, CNRS, UPS, CNES, 9 Av. colonel Roche, BP 44346, 31028 Toulouse Cedex 4, France
[124] MTA CSFK Lendület Near-Field Cosmology Research Group, Konkoly Observatory, MTA Research Centre for Astronomy and Earth Sciences, Konkoly Thege Miklós út 15-17, 1121 Budapest, Hungary
[125] Departmento de Física de la Tierra y Astrofísica, Universidad Complutense de Madrid, 28040 Madrid, Spain
[126] Villanova University, Department of Astrophysics and Planetary Science, 800 E Lancaster Avenue, Villanova, PA 19085, USA
[127] INAF – Osservatorio Astronomico di Brera, via E. Bianchi, 46, 23807 Merate, LC, Italy
[128] STFC, Rutherford Appleton Laboratory, Harwell, Didcot OX11 0QX, UK
[129] Charles University, Faculty of Mathematics and Physics, Astronomical Institute of Charles University, V Holesovickach 2, 18000 Prague, Czech Republic
[130] Department of Particle Physics and Astrophysics, Weizmann Institute of Science, Rehovot 7610001, Israel
[131] Department of Astrophysical Sciences, Princeton University, 4 Ivy Lane, Princeton, NJ 08544, USA
[132] Departamento de Astrofísica, Centro de Astrobiología (CSIC-INTA), ESA-ESAC, Camino Bajo del Castillo s/n, 28692 Villanueva de la Cañada, Madrid, Spain
[133] naXys, University of Namur, Rempart de la Vierge, 5000 Namur, Belgium
[134] CGI Deutschland B.V. & Co. KG, Mornewegstr. 30, 64293 Darmstadt, Germany
[135] Institute of Global Health, University of Geneva, Geneva, Switzerland
[136] Astronomical Observatory Institute, Faculty of Physics, Adam Mickiewicz University, Poznań, Poland
[137] H H Wills Physics Laboratory, University of Bristol, Tyndall Avenue, Bristol BS8 1TL, UK
[138] Department of Physics and Astronomy G. Galilei, University of Padova, Vicolo dell'Osservatorio 3, 35122 Padova, Italy
[139] CERN, Esplanade des Particules 1, PO Box 1211 Geneva, Switzerland
[140] Applied Physics Department, Universidade de Vigo, 36310 Vigo, Spain
[141] Association of Universities for Research in Astronomy, 1331 Pennsylvania Ave. NW, Washington, DC 20004, USA
[142] European Southern Observatory, Alonso de Córdova 3107, Casilla 19, Santiago, Chile
[143] Sorbonne Université, CNRS, UMR7095, Institut d'Astrophysique de Paris, 98bis bd. Arago, 75014 Paris, France
[144] Faculty of Mathematics and Physics, University of Ljubljana, Jadranska ulica 19, 1000 Ljubljana, Slovenia

Appendix A: Acknowledgements

This paper is dedicated to the memory of Arlo U. Landolt (1935–2022) whose contribution to the development of modern astronomical photometry has been invaluable.

We are very grateful to an anonymous Referee for a prompt and constructive report, that improved the quality of the manuscript. We acknowledge also the contribution of the A&A editor T. Forveille for additional insightful comments and suggestions. We are very grateful to many colleagues around the world that gave their help to this project by providing data and guidelines to use them, as well as valuable suggestions and advice. We hope that the following list includes all of them: M.S. Bessell, C. Clementini, E.A. Magnier, P.M. Marrese, A. Mucciarelli, S.J. Murphy, D. Nardiello, P. Stetson, M. Scalco. We apologise for those that we inadvertently forgot to mention. With this work PM, MB, AB and CC acknowledge with gratitude the encouragement of Flavio Fusi Pecci who convinced them to join the adventure of the Gaia mission, seventeen years ago.

The *Gaia* mission and data processing have financially been supported by, in alphabetical order by country:

- the Algerian Centre de Recherche en Astronomie, Astrophysique et Géophysique of Bouzareah Observatory;
- the Austrian Fonds zur Förderung der wissenschaftlichen Forschung (FWF) Hertha Firnberg Programme through grants T359, P20046, and P23737;
- the BELgian federal Science Policy Office (BELSPO) through various PROgramme de Développement d'Expériences scientifiques (PRODEX) grants and the Polish Academy of Sciences – Fonds Wetenschappelijk Onderzoek through grant VS.091.16N, and the Fonds de la Recherche Scientifique (FNRS), and the Research Council of Katholieke Universiteit (KU) Leuven through grant C16/18/005 (Pushing AsteRoseismology to the next level with TESS, GaiA, and the Sloan DIgital Sky SurvEy – PARADISE);
- the Brazil-France exchange programmes Fundação de Amparo à Pesquisa do Estado de São Paulo (FAPESP) and Coordenação de Aperfeicoamento de Pessoal de Nível Superior (CAPES) – Comité Français d'Evaluation de la Coopération Universitaire et Scientifique avec le Brésil (COFECUB);
- the Chilean Agencia Nacional de Investigación y Desarrollo (ANID) through Fondo Nacional de Desarrollo Científico y Tecnológico (FONDECYT) Regular Project 1210992 (L. Chemin);
- the National Natural Science Foundation of China (NSFC) through grants 11573054, 11703065, and 12173069, the China Scholarship Council through grant 201806040200, and the Natural Science Foundation of Shanghai through grant 21ZR1474100;
- the Tenure Track Pilot Programme of the Croatian Science Foundation and the École Polytechnique Fédérale de Lausanne and the project TTP-2018-07-1171 'Mining the Variable Sky', with the funds of the Croatian-Swiss Research Programme;
- the Czech-Republic Ministry of Education, Youth, and Sports through grant LG 15010 and INTER-EXCELLENCE grant LTAUSA18093, and the Czech Space Office through ESA PECS contract 98058;
- the Danish Ministry of Science;
- the Estonian Ministry of Education and Research through grant IUT40-1;
- the European Commission?s Sixth Framework Programme through the European Leadership in Space Astrometry (ELSA) Marie Curie Research Training Network (MRTN-CT-2006-033481), through Marie Curie project PIOF-GA-2009-255267 (Space AsteroSeismology & RR Lyrae stars, SAS-RRL), and through a Marie Curie Transfer-of-Knowledge (ToK) fellowship (MTKD-CT-2004-014188); the European Commission's Seventh Framework Programme through grant FP7-606740 (FP7-SPACE-2013-1) for the *Gaia* European Network for Improved data User Services (GENIUS) and through grant 264895 for the *Gaia* Research for European Astronomy Training (GREAT-ITN) network;
- the European Cooperation in Science and Technology (COST) through COST Action CA18104 'Revealing the Milky Way with *Gaia* (MW-Gaia)';
- the European Research Council (ERC) through grants 320360, 647208, and 834148 and through the European Union?s Horizon 2020 research and innovation and excellent science programmes through Marie Skłodowska-Curie grant 745617 (Our Galaxy at full HD – Gal-HD) and 895174 (The build-up and fate of self-gravitating systems in the Universe) as well as grants 687378 (Small Bodies: Near and Far), 682115 (Using the Magellanic Clouds to Understand the Interaction of Galaxies), 695099 (A sub-percent distance scale from binaries and Cepheids – CepBin), 716155 (Structured ACCREtion Disks – SACCRED), 951549 (Sub-percent calibration of the extragalactic distance scale in the era of big surveys – UniverScale), and 101004214 (Innovative Scientific Data Exploration and Exploitation Applications for Space Sciences – EXPLORE);
- the European Science Foundation (ESF), in the framework of the *Gaia* Research for European Astronomy Training Research Network Programme (GREAT-ESF);
- the European Space Agency (ESA) in the framework of the *Gaia* project, through the Plan for European Cooperating States (PECS) programme through contracts C98090 and 4000106398/12/NL/KML for Hungary, through contract 4000115263/15/NL/IB for Germany, and through PROgramme de Développement d'Expériences scientifiques (PRODEX) grant 4000127986 for Slovenia;
- the Academy of Finland through grants 299543, 307157, 325805, 328654, 336546, and 345115 and the Magnus Ehrnrooth Foundation;
- the French Centre National d?Études Spatiales (CNES), the Agence Nationale de la Recherche (ANR) through grant ANR-10-IDEX-0001-02 for the 'Investissements d'avenir' programme, through grant ANR-15-CE31-0007 for project 'Modelling the Milky Way in the *Gaia* era? (MOD4Gaia), through grant ANR-14-CE33-0014-01 for project 'The Milky Way disc formation in the *Gaia* era? (ARCHEOGAL), through grant ANR-15-CE31-0012-01 for project 'Unlocking the potential of Cepheids as primary distance calibrators? (UnlockCepheids), through grant ANR-19-CE31-0017 for project 'Secular evolution of galxies' (SEGAL), and through grant ANR-18-CE31-0006 for project 'Galactic Dark Matter' (GaDaMa), the Centre National de la Recherche Scientifique (CNRS) and its SNO *Gaia* of the Institut des Sciences de l?Univers (INSU), its Programmes Nationaux: Cosmologie et Galaxies (PNCG), Gravitation Références Astronomie Métrologie (PNGRAM), Planétologie (PNP), Physique et Chimie du Milieu Interstellaire (PCMI), and Physique Stellaire (PNPS), the 'Action Fédératrice *Gaia*' of the Observatoire de Paris, the Région de Franche-Comté, the Institut National Polytechnique (INP) and the Institut National

de Physique nucléaire et de Physique des Particules (IN2P3) co-funded by CNES;
– the German Aerospace Agency (Deutsches Zentrum für Luft- und Raumfahrt e.V., DLR) through grants 50QG0501, 50QG0601, 50QG0602, 50QG0701, 50QG0901, 50QG1001, 50QG1101, 50QG1401, 50QG1402, 50QG1403, 50QG1404, 50QG1904, 50QG2101, 50QG2102, and 50QG2202, and the Centre for Information Services and High Performance Computing (ZIH) at the Technische Universität Dresden for generous allocations of computer time;
– the Hungarian Academy of Sciences through the Lendület Programme grants LP2014-17 and LP2018-7 and the Hungarian National Research, Development, and Innovation Office (NKFIH) through grant KKP-137523 ('SeismoLab');
– the Science Foundation Ireland (SFI) through a Royal Society – SFI University Research Fellowship (M. Fraser);
– the Israel Ministry of Science and Technology through grant 3-18143 and the Tel Aviv University Center for Artificial Intelligence and Data Science (TAD) through a grant;
– the Agenzia Spaziale Italiana (ASI) through contracts I/037/08/0, I/058/10/0, 2014-025-R.0, 2014-025-R.1.2015, and 2018-24-HH.0 to the Italian Istituto Nazionale di Astrofisica (INAF), contract 2014-049-R.0/1/2 to INAF for the Space Science Data Centre (SSDC, formerly known as the ASI Science Data Center, ASDC), contracts I/008/10/0, 2013/030/I.0, 2013-030-I.0.1-2015, and 2016-17-I.0 to the Aerospace Logistics Technology Engineering Company (ALTEC S.p.A.), INAF, and the Italian Ministry of Education, University, and Research (Ministero dell'Istruzione, dell'Università e della Ricerca) through the Premiale project 'MIning The Cosmos Big Data and Innovative Italian Technology for Frontier Astrophysics and Cosmology' (MITiC);
– the Netherlands Organisation for Scientific Research (NWO) through grant NWO-M-614.061.414, through a VICI grant (A. Helmi), and through a Spinoza prize (A. Helmi), and the Netherlands Research School for Astronomy (NOVA);
– the Polish National Science Centre through HARMONIA grant 2018/30/M/ST9/00311 and DAINA grant 2017/27/L/ST9/03221 and the Ministry of Science and Higher Education (MNiSW) through grant DIR/WK/2018/12;
– the Portuguese Fundação para a Ciência e a Tecnologia (FCT) through national funds, grants SFRH/BD/128840/2017 and PTDC/FIS-AST/30389/2017, and work contract DL 57/2016/CP1364/CT0006, the Fundo Europeu de Desenvolvimento Regional (FEDER) through grant POCI-01-0145-FEDER-030389 and its Programa Operacional Competitividade e Internacionalização (COMPETE2020) through grants UIDB/04434/2020 and UIDP/04434/2020, and the Strategic Programme UIDB/00099/2020 for the Centro de Astrofísica e Gravitação (CENTRA);
– the Slovenian Research Agency through grant P1-0188;
– the Spanish Ministry of Economy (MINECO/FEDER, UE), the Spanish Ministry of Science and Innovation (MICIN), the Spanish Ministry of Education, Culture, and Sports, and the Spanish Government through grants BES-2016-078499, BES-2017-083126, BES-C-2017-0085, ESP2016-80079-C2-1-R, ESP2016-80079-C2-2-R, FPU16/03827, PDC2021-121059-C22, RTI2018-095076-B-C22, and TIN2015-65316-P ('Computación de Altas Prestaciones VII'), the Juan de la Cierva Incorporación Programme (FJCI-2015-2671 and IJC2019-04862-I for F. Anders), the Severo Ochoa Centre of Excellence Programme (SEV2015-0493), and MICIN/AEI/10.13039/501100011033 (and the European Union through European Regional Development Fund 'A way of making Europe') through grant RTI2018-095076-B-C21, the Institute of Cosmos Sciences University of Barcelona (ICCUB, Unidad de Excelencia 'María de Maeztu?) through grant CEX2019-000918-M, the University of Barcelona's official doctoral programme for the development of an R+D+i project through an Ajuts de Personal Investigador en Formació (APIF) grant, the Spanish Virtual Observatory through project AyA2017-84089, the Galician Regional Government, Xunta de Galicia, through grants ED431B-2021/36, ED481A-2019/155, and ED481A-2021/296, the Centro de Investigación en Tecnologías de la Información y las Comunicaciones (CITIC), funded by the Xunta de Galicia and the European Union (European Regional Development Fund – Galicia 2014-2020 Programme), through grant ED431G-2019/01, the Red Española de Supercomputación (RES) computer resources at MareNostrum, the Barcelona Supercomputing Centre - Centro Nacional de Supercomputación (BSC-CNS) through activities AECT-2017-2-0002, AECT-2017-3-0006, AECT-2018-1-0017, AECT-2018-2-0013, AECT-2018-3-0011, AECT-2019-1-0010, AECT-2019-2-0014, AECT-2019-3-0003, AECT-2020-1-0004, and DATA-2020-1-0010, the Departament d'Innovació, Universitats i Empresa de la Generalitat de Catalunya through grant 2014-SGR-1051 for project 'Models de Programació i Entorns d'Execució Parallels' (MPEXPAR), and Ramon y Cajal Fellowship RYC2018-025968-I funded by MICIN/AEI/10.13039/501100011033 and the European Science Foundation ('Investing in your future');
– the Swedish National Space Agency (SNSA/Rymdstyrelsen);
– the Swiss State Secretariat for Education, Research, and Innovation through the Swiss Activités Nationales Complémentaires and the Swiss National Science Foundation through an Eccellenza Professorial Fellowship (award PCEFP2_194638 for R. Anderson);
– the United Kingdom Particle Physics and Astronomy Research Council (PPARC), the United Kingdom Science and Technology Facilities Council (STFC), and the United Kingdom Space Agency (UKSA) through the following grants to the University of Bristol, the University of Cambridge, the University of Edinburgh, the University of Leicester, the Mullard Space Sciences Laboratory of University College London, and the United Kingdom Rutherford Appleton Laboratory (RAL): PP/D006511/1, PP/D006546/1, PP/D006570/1, ST/I000852/1, ST/J005045/1, ST/K00056X/1, ST/K000209/1, ST/K000756/1, ST/L006561/1, ST/N000595/1, ST/N000641/1, ST/N000978/1, ST/N001117/1, ST/S000089/1, ST/S000976/1, ST/S000984/1, ST/S001123/1, ST/S001948/1, ST/S001980/1, ST/S002103/1, ST/V000969/1, ST/W002469/1, ST/W002493/1, ST/W002671/1, ST/W002809/1, and EP/V520342/1.

The *Gaia* project and data processing have made use of:
– the Set of Identifications, Measurements, and Bibliography for Astronomical Data (SIMBAD, Wenger et al. 2000), the 'Aladin sky atlas' (Bonnarel et al. 2000; Boch & Fernique 2014), and the VizieR catalogue access tool (Ochsenbein et al. 2000), all operated at the Centre de Données astronomiques de Strasbourg (CDS);

– the National Aeronautics and Space Administration (NASA) Astrophysics Data System (ADS);
– the SPace ENVironment Information System (SPENVIS), initiated by the Space Environment and Effects Section (TEC-EES) of ESA and developed by the Belgian Institute for Space Aeronomy (BIRA-IASB) under ESA contract through ESA?s General Support Technologies Programme (GSTP), administered by the BELgian federal Science Policy Office (BELSPO);
– the Spanish Virtual Observatory (https://svo.cab.inta-csic.es) project funded by MCIN/AEI/10.13039/501100011033/ through grant PID2020-112949GB-I00 (Rodrigo & Solano 2020);
– the software products TOPCAT, STIL, and STILTS (Taylor 2005, 2006b);
– Matplotlib (Hunter 2007);
– IPython (Pérez & Granger 2007);
– Astropy, a community-developed core Python package for Astronomy (Astropy Collaboration 2018);
– NumPy (Harris et al. 2020);
– pyphot (http://github.com/mfouesneau/pyphot);
– R (R Core Team 2013);
– the HIPPARCOS-2 catalogue (van Leeuwen 2007). The HIPPARCOS and Thyco catalogues were constructed under the responsibility of large scientific teams collaborating with ESA. The Consortia Leaders were Lennart Lindegren (Lund, Sweden: NDAC) and Jean Kovalevsky (Grasse, France: FAST), together responsible for the HIPPARCOS Catalogue; Erik Høg (Copenhagen, Denmark: TDAC) responsible for the Thyco Catalogue; and Catherine Turon (Meudon, France: INCA) responsible for the HIPPARCOS Input Catalogue (HIC);
– the Thyco 2 catalogue (Høg et al. 2000), the construction of which was supported by the Velux Foundation of 1981 and the Danish Space Board;
– The Tycho double star catalogue (TDSC, Fabricius et al. 2002), based on observations made with the ESA HIPPARCOS astrometry satellite, as supported by the Danish Space Board and the United States Naval Observatory through their double-star programme;
– the first data release of the Pan-STARRS survey (Chambers et al. 2016; Magnier et al. 2020b; Waters et al. 2020; Magnier et al. 2020c,a; Flewelling et al. 2020). The Pan-STARRS1 Surveys (PS1) and the PS1 public science archive have been made possible through contributions by the Institute for Astronomy, the University of Hawaii, the Pan-STARRS Project Office, the Max-Planck Society and its participating institutes, the Max Planck Institute for Astronomy, Heidelberg and the Max Planck Institute for Extraterrestrial Physics, Garching, The Johns Hopkins University, Durham University, the University of Edinburgh, the Queen's University Belfast, the Harvard-Smithsonian Center for Astrophysics, the Las Cumbres Observatory Global Telescope Network Incorporated, the National Central University of Taiwan, the Space Telescope Science Institute, the National Aeronautics and Space Administration (NASA) through grant NNX08AR22G issued through the Planetary Science Division of the NASA Science Mission Directorate, the National Science Foundation through grant AST-1238877, the University of Maryland, Eotvos Lorand University (ELTE), the Los Alamos National Laboratory, and the Gordon and Betty Moore Foundation;
– the fifteenth and the sixteenth data releases of the Sloan Digitial Sky Survey, (SDSS DR15, Blanton et al. 2017) and (SDSS DR16, Ahumada et al. 2020). Funding for the Sloan Digital Sky Survey IV has been provided by the Alfred P. Sloan Foundation, the US Department of Energy Office of Science, and the Participating Institutions. SDSS-IV acknowledges support and resources from the Center for High Performance Computing at the University of Utah. The SDSS website is www.sdss.org. SDSS-IV is managed by the Astrophysical Research Consortium for the Participating Institutions of the SDSS Collaboration including the Brazilian Participation Group, the Carnegie Institution for Science, Carnegie Mellon University, Center for Astrophysics | Harvard & Smithsonian, the Chilean Participation Group, the French Participation Group, Instituto de Astrofísica de Canarias, The Johns Hopkins University, Kavli Institute for the Physics and Mathematics of the Universe (IPMU)/University of Tokyo, the Korean Participation Group, Lawrence Berkeley National Laboratory, Leibniz Institut für Astrophysik Potsdam (AIP), Max-Planck-Institut für Astronomie (MPIA Heidelberg), Max-Planck-Institut für Astrophysik (MPA Garching), Max-Planck-Institut für Extraterrestrische Physik (MPE), National Astronomical Observatories of China, New Mexico State University, New York University, University of Notre Dame, Observatário Nacional/MCTI, The Ohio State University, Pennsylvania State University, Shanghai Astronomical Observatory, United Kingdom Participation Group, Universidad Nacional Autónoma de México, University of Arizona, University of Colorado Boulder, University of Oxford, University of Portsmouth, University of Utah, University of Virginia, University of Washington, University of Wisconsin, Vanderbilt University, and Yale University.
– the second release of the SkyMapper catalogue (SkyMapper DR2, Onken et al. 2019, Digital Object Identifier 10.25914/5ce60d31ce759). The national facility capability for SkyMapper has been funded through grant LE130100104 from the Australian Research Council (ARC) Linkage Infrastructure, Equipment, and Facilities (LIEF) programme, awarded to the University of Sydney, the Australian National University, Swinburne University of Technology, the University of Queensland, the University of Western Australia, the University of Melbourne, Curtin University of Technology, Monash University, and the Australian Astronomical Observatory. SkyMapper is owned and operated by The Australian National University's Research School of Astronomy and Astrophysics. The survey data were processed and provided by the SkyMapper Team at the the Australian National University. The SkyMapper node of the All-Sky Virtual Observatory (ASVO) is hosted at the National Computational Infrastructure (NCI). Development and support the SkyMapper node of the ASVO has been funded in part by Astronomy Australia Limited (AAL) and the Australian Government through the Commonwealth's Education Investment Fund (EIF) and National Collaborative Research Infrastructure Strategy (NCRIS), particularly the National eResearch Collaboration Tools and Resources (NeCTAR) and the Australian National Data Service Projects (ANDS);

The GBOT programme uses observations collected at (i) the European Organisation for Astronomical Research in the Southern Hemisphere (ESO) with the VLT Survey Telescope (VST), under ESO programmes 092.B-0165, 093.B-0236, 094.B-0181, 095.B-0046, 096.B-0162, 097.B-0304, 098.B-0030, 099.B-0034, 0100.B-0131, 0101.B-0156, 0102.B-0174, and 0103.B-0165; and (ii) the Liverpool Telescope, which is operated on

the island of La Palma by Liverpool John Moores University in the Spanish Observatorio del Roque de los Muchachos of the Instituto de Astrofísica de Canarias with financial support from the United Kingdom Science and Technology Facilities Council, and (iii) telescopes of the Las Cumbres Observatory Global Telescope Network.

Appendix B: Minimum width of flux-conserving passbands and suggestions for line photometry

In general, the flux through a given passband can be correctly measured from XPSP only if the characteristic width of the TC is larger than the LSF of the EC XP spectrum in the wavelength range of the passband. To trace the relation between passband width and LSF width we adopt the following simple parameter:

$$Rf = \frac{FWHM_{passband}(\lambda_0)}{FWHM_{LSF}(\lambda_0)}, \tag{B.1}$$

which is the ratio between the FWHM of the passband and of the XP LSF at the central/peak wavelength of the passband λ_0, where the relevant ECS XP LSF width should be taken from Montegriffo et al. (2023). This simple parameter cannot take into account all the subtleties of the relation we are considering, that is, the FWHM is not fully adequate to describe asymmetric TCs. However, here it is sufficient to address the core of this problem and to provide a simple and general criterion for flux conservation and reproducibility of magnitudes in existing systems.

In principle, for symmetric passbands and local symmetric and perfectly modelled LSF, $Rf > 1$ should guarantee that all the incoming flux through the considered TC can be correctly measured by XPSP in any case. However, the LSF is not symmetric (Montegriffo et al. 2023), the instrument model that is used to transform XP mean spectra into EC is not perfect and, consequently, the mixing between photons of different wavelengths –which is intrinsic to slit-less spectroscopy– is not optimally corrected.

To derive an empirical criterion defining the minimum Rf of a passband whose XPSP correctly measure and/or conserve the flux, we proceed as follows. Consider a spectral feature that is very narrow with respect to the local XP LSF, for example the stellar Hα Balmer line, and suppose we attempt to measure the flux in a portion of the spectrum including the line with XPSP using a passband with $Rf < 1$. If the source has Hα in emission, the XP LSF will move a fraction of photons from the line out of the range covered by the passband, resulting in a loss of Hα flux. Photons outside that range would also leak within the passband for the same reason, but the asymmetry between the excess flux in the line and the lower surrounding continuum would end up in a net flux loss. The opposite would happen for Hα in absorption: in this case, the asymmetry between the deficit of photons in the line and the flat but higher continuum level outside the passband will lead to the measurement of a spurious excess of flux in the passband, mimicking a lower depth of the line.

The idea is to take a set of stars for which we have EC XP spectra and their external counterparts at much higher spectral resolution (HR spectra[31]; in the specific case, about $R \simeq 1000$, to be compared with $R \simeq 30 - 80$ of XP ECS) and to compare synthetic photometry from the two source spectra around strong spectral lines using passbands of various width. Dealing with absorption features in the presence of strong lines, the fluxes through an overly narrow passband will be larger when measured from XP than from HR spectra, corresponding to positive magnitude differences $\mathrm{mag}_{HR} - \mathrm{mag}_{XP}$. Then, progressively wider passbands can be tested until the magnitude difference becomes null, thus identifying the lower Rf limit allowing correct measurement of the flux in the presence of a strong spectral feature.

Here we perform this test with a set of custom synthetic passbands centred on Hβ ($FWHM_{LSF} = 12.6$ nm) and Hα ($FWHM_{LSF} = 8.4$ nm), with FWHM ranging from 1 nm to 25 nm. TCs are centred at the wavelength of the corresponding line and have a strictly symmetric shape, being the junction of two error functions.

The sample is composed of the calibrating and validating sets of stars including the Gaia SPSS and the PVL (Pancino et al. 2021) and the selection of NGSL stars (Heap & Lindler 2016)

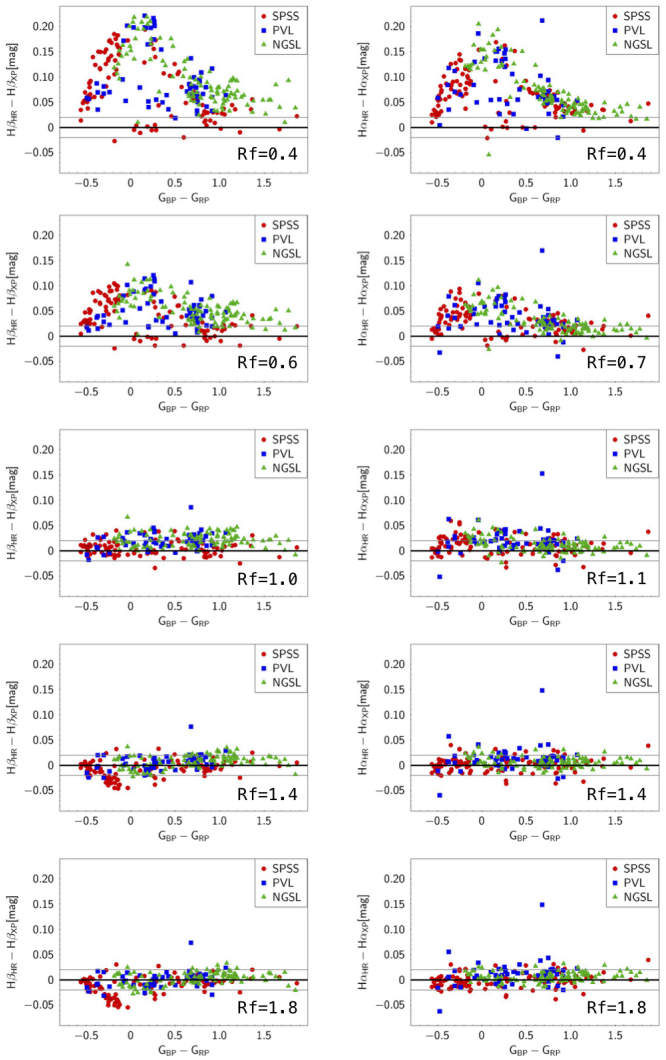

Fig. B.1. Difference in synthetic magnitudes from HR and XP spectra for SPSS, PVL, and selected NGSL using passbands of increasing FWHM (from top to bottom) to measure the flux around Hβ (left panels) and Hα (right panels), as a function of G_{BP}-G_{RP} colour. The passbands FWHM adopted in the various panels are, from top to bottom, 5, 8, 13, 18, 23 nm (Hβ), and 3, 6, 9, 12, 15 nm (Hα). The corresponding Rf values are reported in each panel.

[31] We note that synthetic photometry from HR spectra, in this context, is fully equivalent to external direct photometry obtained by imaging with photometric filters. The conclusions reached in this section are fully applicable to narrow-line photometry obtained in this way, as, e.g. in IPHAS (Drew et al. 2005) or the VST Photometric Hα Survey (VPHAS+, Drew et al. 2014).

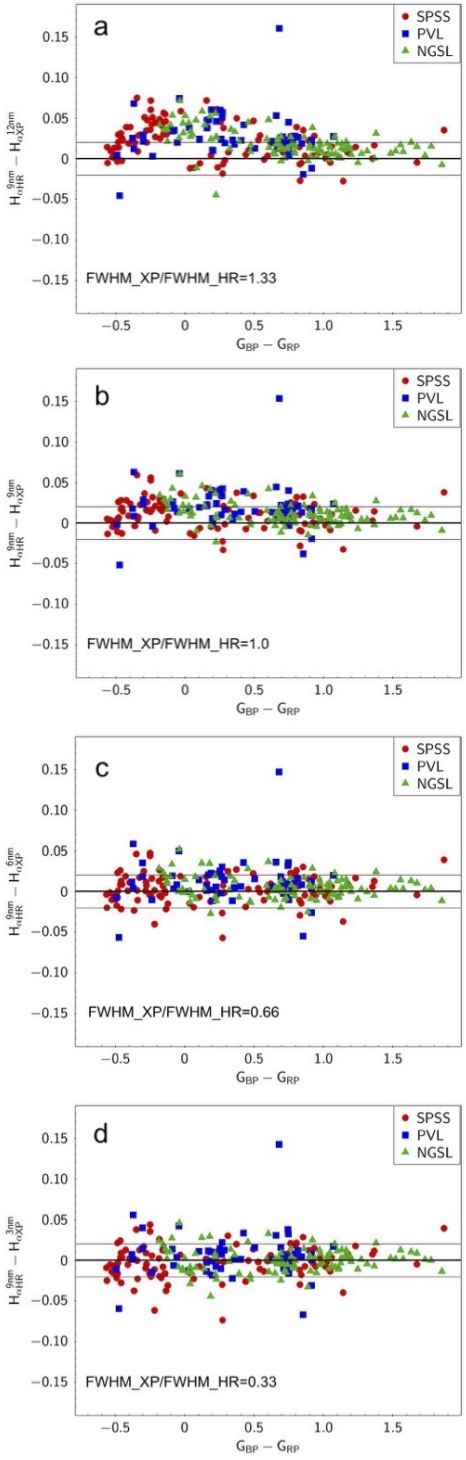

Fig. B.2. Difference of synthetic Hα magnitudes from HR and XP spectra for SPSS, PVL, and selected NGSL as a function of $G_{\rm BP} - G_{\rm RP}$ colour. In this case, the width of the TC adopted for synthetic photometry on HR spectra is kept fixed ($FWHM = 9.0$ nm), while the width of the TC used for synthetic photometry on XP spectra is varied from $FWHM = 12.0$ nm to $FWHM = 9.0, 6.0, 3.0$ nm, from top to bottom. The various panels are labelled according to the ratio between the FWHM of the XP and HR TCs.

adopted by Montegriffo et al. (2023). AB magnitudes are considered as they directly trace fluxes.

Figure B.1 illustrates the procedure. In the upper pair of panels, passbands significantly narrower than the local LSF are adopted ($Rf = 0.4$). Consequently, for the majority of stars, the difference between HR and XP synthetic magnitudes increases from G_{BP}-$G_{RP} \simeq -0.5$ to G_{BP}-$G_{RP} \simeq 0.0$, reaching its maximum for stars displaying the maximum strength of Balmer absorption lines (A stars; the handful of exceptions are DC and DB WDs with the colour of A stars but lacking strong H lines in their spectra). Then the magnitude difference begins to decrease, reaching a null value for $BP-RP > 1.0$, for spectral types later than G. As passbands with larger Rf are adopted, the amplitude of the arch of the magnitude difference decreases, until they reach $\simeq 0.0$ over the considered colour range at $Rf \simeq 1.4$, remaining there for larger values of Rf. It is important to note that the amplitude of the discrepancy is already as low as $\simeq 0.01 - 0.02$ mag around $Rf = 1.0 - 1.1$. Still, we prefer to provide a conservative general criterion, possibly accounting also for the approximations involved.

The conclusion of this experiment is that synthetic fluxes and magnitudes can be accurately measured from EC XP spectra only adopting passbands with $Rf \geq 1.4$. This implies, that magnitudes from existing systems can be accurately reproduced only if this condition is satisfied, if the TC of the existing system is adopted to obtain the corresponding XPSP (see below for a different approach that may help to circumvent this rule). It is reassuring that the same result is consistently found when testing two spectral features that are measured in the different instruments that are used to get mean XP spectra, i.e. BP and (mainly) RP for Hβ and Hα, respectively. Moreover, in regions of the spectrum lacking strong features, the flux is conserved in XPSP also using passbands with $Rf < 1.4$, because, in the absence of any strong flux asymmetry, the losses from inside the passband are compensated by the leaks from outside the passband, leaving the balance near the equilibrium.

The above conclusions refer to the comparison between photometry obtained from different spectra *with the same TCs*. However, following up the results shown in Sect. 4.3, now we compare Hα magnitudes obtained with a $FWHM = 9$ nm TC ($Rf = 1.1$) from the HR spectra with those obtained from XP spectra using TCs of various width, in particular $FWHM = 12, 9, 6, 3$ nm. The results of this experiment are presented in Fig. B.2. When the passband adopted for the XPSP is wider than that taken as reference for the HR SP (panel a), the distribution is fully analogous to that seen in Fig. B.1 for $Rf < 1.0$, as, also in this case, the signal from the line is diluted by the continuum. In that case, the dilution was produced by an asymmetric exchange of photons at the thresholds of a passband that is narrower than the local LSF. Here it is due to the inclusion of larger portions of the continuum in the passband adopted for the XP spectra than in the one adopted for the HR spectra. When, as in panel (b), the same passband is adopted in both cases, the performance is determined by the Rf, as already established in the previous experiment. However, the comparisons shown in panels (c) and (d) of Fig. B.2 show that the HR photometry can be satisfactorily matched even for $Rf < 1.4$, with XPSP obtained with a narrower TC than that adopted for the HR spectra. In such a case, the increased sensitivity of the narrower passband offsets the flux lost outside of the passband edges. In the limit of the narrowest synthetic passband, the quantity measured is the height of the line relative to the continuum, after it is convolved with the LSF. A limited set of experiments as well as simple models suggest that with this approach, narrow line photometry in presence of strong spectral features can be reproduced with XPSP down to $Rf \gtrsim 1.0$. In these cases, the best choice of the width of the TC to be adopted for the XPSP should be determined with experiments like those shown in Fig. B.2, taking into account the LSF

at the wavelength of the considered line and the TC adopted by the survey that one intend to calibrate with *Gaia* XPSP. Finally, it is worth noting that while passbands with $Rf < 1.0$ cannot conserve or reliably trace the flux of an emission line, they can still carry useful information on the spectral feature they are targeting.

Appendix C: Comparisons with stellar models

In this section, we use stellar models to assess the quality of five standardised photometry systems (Johnson, Pan-STARRS1, SDSS, Strömgren, HST ACS/WFC). We compare the photometry of seven OCs presented in Table C.1 with the expectations from theoretical isochrones.

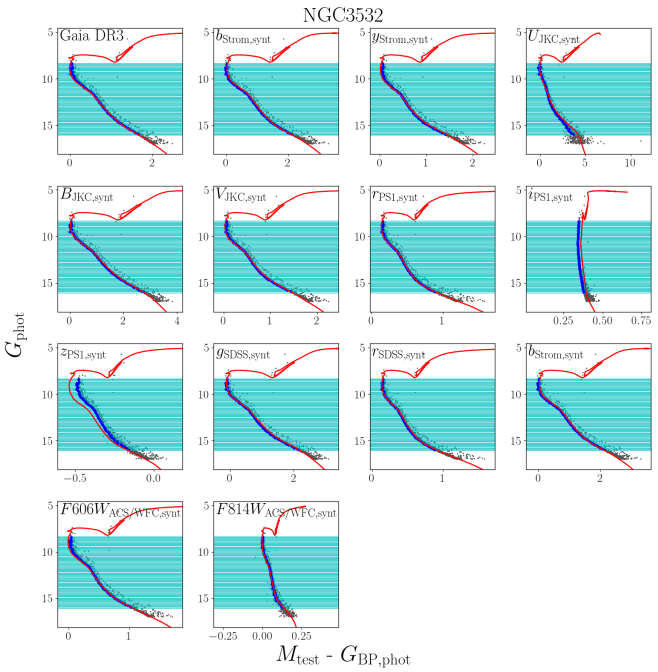

Fig. C.1. Example of isochrone fitting on the cluster NGC 3532. The first panel is *Gaia* CMD while the other CMD contained several synthetic bands from Johnson (B, V), Pan-STARRS1 (r, i, z), SLOAN (u, g, r). The red line is the PARSEC isochrone, the cyan lines show the binning definition (see C), and the blue dots are the bluer edge of the colour (x axis) of the stellar distribution.

The set of theoretical isochrones used for the comparison are taken from the PARSEC library[32] v2.1 (the PAdova and TRieste Stellar Evolution Code; Bressan et al. 2012). The bolometric correction were calculated using the online tool YBC[33] (PARSEC Bolometric Correction; Chen et al. 2019), which interpolates a series of pre-computed bolometric correction tables in $T_{\rm eff}$, [Fe/H], $\log g$, and $E(B-V)$. For this work, we use exclusively the calculation performed on the Phoenix synthetic spectra (Allard et al. 2013).

Cluster parameters are taken from the literature (e.g. from the catalogue in Bossini et al. 2019, and summarised in Table C.1). First, we verify the agreement of the isochrone on the observational CMD in the passbands G against $G_{\rm BP}-G_{\rm RP}$. Then we compare the isochrones with the standardised photometric bands.

An example can be seen in figure C.1 for the OC NGC 3532, where we also show our procedure. We first divide the main

[32] http://stev.oapd.inaf.it/cgi-bin/cmd
[33] http://stev.oapd.inaf.it/YBC/index.html

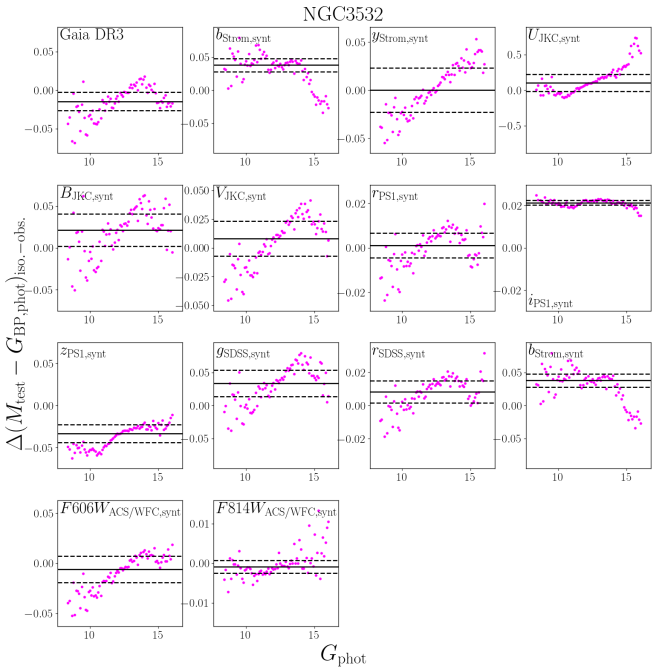

Fig. C.2. Residuals between the isochrone and the bluer edge of the colour (x axis) in the Fig. C.1 CMDs. The back solid line is the median of the deviations while the dashed line represents the MAD.

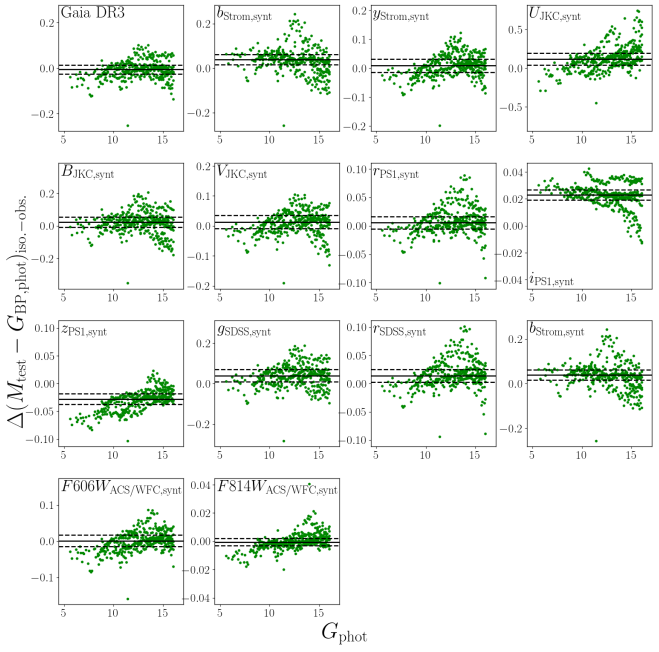

Fig. C.3. As in Fig. C.2: Residuals between the isochrone and the data for the selected OCs. The back solid line is the median of the deviations while the dashed line represents the MAD.

sequence along the G magnitude in bin of 0.1 mag from the turn-off down to $G = 16.00$ (blue lines panel). For each bin, we select the blue edge of the main sequence and compare the standardised photometry in JKC, PS1, ACS/WFC, SDSS, and Strömgren systems with isochrone expectations. This procedure allows us to avoid contamination by unresolved binaries and differential reddening that could have blurred the distribution toward the red. In nearby clusters such as Pleiades, we discard faint main sequence

Table C.1. Adopted parameters for the sample of open clusters.

cluster	log(*age*) dex	$m-M$ mag	E(B-V) mag	[Fe/H] dex
NGC2168	8.60	9.33	0.15	-0.21
M44	8.87	6.35	0.03	0.07
M67	9.56	9.73	0.04	0.00
NGC2447	8.75	10.09	0.03	0.00
NGC3532	8.60	8.43	0.02	0.00
NGC6791	9.93	13.08	0.10	0.40
NGC6819	9.30	12.16	0.15	0.00
Pleiades	7.94	5.67	0.05	0.00

Table C.2. Median and MAD of the residuals between the isochrone and the bluer edge of the colour (x axis) in the Fig. C.1 CMDs for all the tested photometry against $G_{\rm RP,phot}$ in all seven open clusters.

Photometric band	median mag	MAD mag
$G_{\rm BP,phot}$	-0.005	0.020
$b_{\rm Strom,synt}$	0.039	0.023
$y_{\rm Strom,synt}$	0.009	0.023
$U_{\rm JKC,synt}$	0.116	0.076
$B_{\rm JKC,synt}$	0.023	0.032
$V_{\rm JKC,synt}$	0.013	0.022
$r_{\rm PS1,synt}$	0.005	0.011
$i_{\rm PS1,synt}$	0.023	0.004
$z_{\rm PS1,synt}$	-0.028	0.010
$g_{\rm SDSS,synt}$	0.039	0.031
$r_{\rm SDSS,synt}$	0.014	0.011
$b_{\rm Strom,synt}$	0.039	0.023
$F606W_{\rm ACS/WFC,synt}$	0.001	0.016
$F814W_{\rm ACS/WFC,synt}$	-0.001	0.003

stars, since it is well known that stellar models do not reproduce the colours of low mass stars. The residuals to the isochrones are reported in figure C.2 for two passbands in each photometric systems. A similar test is performed on each of the selected OCs on a total of 4165 stars. The residuals are shown in figure C.3, while Table C.2 presents the median and median absolute deviation (MAD) of the residual distributions in all the tested passbands for the whole sample.

The agreement is good. Deviations are of the order of a few hundredths of a magnitude, and reach 0.12 mag for $U_{\rm JKC,synt}$.

Appendix D: XPSP of red giants in the SDSS system

The Thanjavur et al. (2021) SDSS Stripe 82 standards sample contains relatively few red giants (approximately 1800). In order to explore the behaviour of standardised SDSS XPSP in the regime of red giants we selected an additional sample of sources from the SDSS Data Release 17 `PhotObjAll` by applying the following cuts:

- 13<`psfmag_{u,g,r,i,z}`<25
- `psfmagerr_{u,g,r,i,z}`<1
- `type==6`
- `psfprob>0`
- `ndetect==nobserve`
- `clean==1`
- `BRIGHT & EDGE & BLENDED & SATURATED & INTERP_CENTER & SATURATED_CENTER & PSF_FLUX_INTERP` flags set to 0.

Additionally, we apply the Gaia filters described above with the addition of:

- `parallax/parallax_error>10.0`
- `in_dr3==True`
- $1.72(G_{BP}-G_{RP})+0.7 > M_G$,

where the last filter describes the linear selection of red giants from the colour–absolute magnitude (designated M_G) diagram. The absolute magnitudes were derived from photo-geometric distances published by Bailer-Jones et al. (2021). The final sample contains almost 74 714 candidate red giant stars, half of which within $\simeq$ 3.2 kpc of the Sun, and more than 95% of which within $\simeq$ 5.0 kpc. These stars are distributed from the base of the RGB to just above the Red Clump and in the colour range $1.0 < G_{BP}-G_{RP} < 5.2$, with $\simeq$ 98% of the sources having $G_{BP}-G_{RP} < 3.0$. The extension to very red colours is mainly due to relatively large interstellar extinction values.

The usual plots of Δmag as a function of G mag and $G_{BP}-G_{RP}$ colour for this sample are presented in Fig. D.1. The typical scatter is larger than for the T21 reference sample, $\sigma \simeq 20$ mmag instead of $\sigma \simeq 10$ mmag at $G = 15.2$,

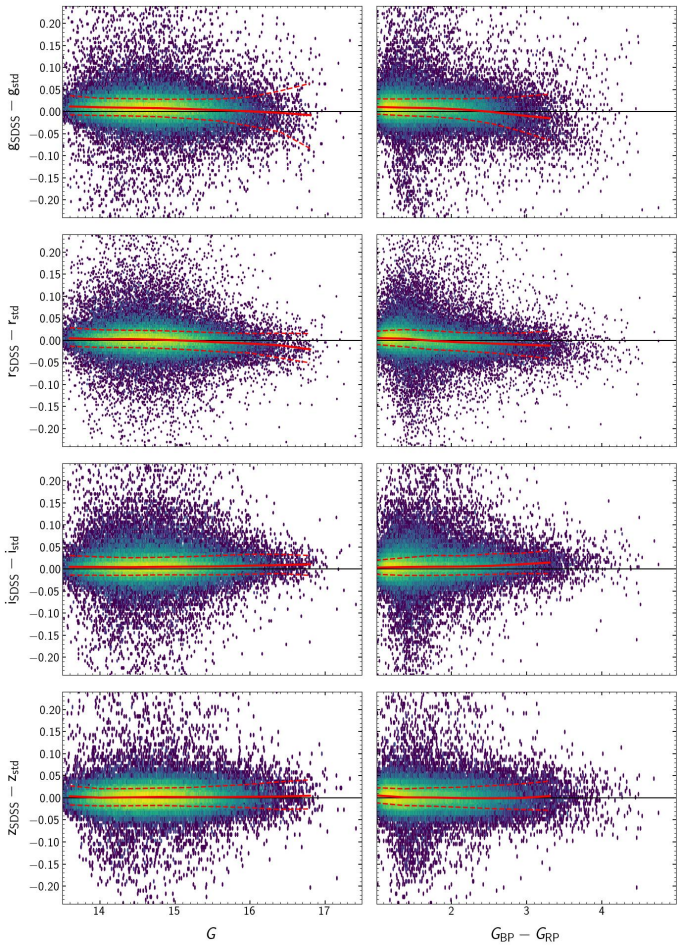

Fig. D.1. Validation of the performance of the synthetic SDSS *griz* bands using the red giant sample sample described in Sect. D. The arrangement of the plots and symbols follows the convention used in Fig. 6. The sources in the sample are restricted to those with $G <$ 17.65 mag and `in_dr3` flag set to 1.

likely owing to the much higher precision of the T21 Stripe 82 photometry with respect to that available over the entire SDSS area in DR17. However, for *riz* bands, the median Δmag is within a few millimag of zero over most of the colour range covered by the sample, and in any case within $\lesssim$ 10.0 mmag, while a colour term of amplitude $\simeq$ 10.0 mmag in the range $1.0 \lesssim G_{BP} - G_{RP} \lesssim 2.5$, reaching an amplitude of $\simeq$ 20.0 mmag in the range $1.0 \lesssim G_{BP} - G_{RP} \lesssim 3.5$ is apparent for the more problematic *g* band (see Sect. 3.1). In *u* band (not shown here), the median Δmag remains below 10 mmag for $G_{BP} - G_{RP} \leq 1.7$, with $\sigma \leq 150$ mmag in that range. For $G_{BP} - G_{RP} > 1.7$, the median difference diverges rapidly. However, only very few sources with `flux_u/flux_error_u>30` can be found in this red realm.

In summary, the results of this validation experiment suggest that the standardisation of SDSS XPSP we obtained from the dwarf-dominated T21 reference sample should also be valid for red giants, with typical accuracy of better than 0.01 mag over a large range of colours. However, it is worth noting that this test is mostly limited to K spectral type, and does not probe the coolest M giants.

Appendix E: Comparison with Stetson's JKC secondary standard stars

In Fig. E.1 we validate XPSP in the standardised JKC system against the subsample of the (Stetson et al. 2019) secondary standard stars described in Sect. 3.2, hereafter referred to as Stetson's validating sample. The comparison is limited to the sources with XP spectra released in DR3 and G<17.65.

For $G_{BP} - G_{RP} < 3.0$, the median of the residuals in V, R, and I magnitudes is within ≃1% of zero, with typical $\sigma \simeq 0.02 - 0.03$ mag. For $G_{BP} - G_{RP} > 3.0$ a significant trend with colour is observed in I band, reaching an amplitude of ≃0.1 mag around $G_{BP} - G_{RP} \simeq 5.0$.

The bifurcation occurring in ΔR for $G_{BP} - G_{RP} \gtrsim 2.5$ should probably be attributed to the heterogeneity of R TCs used in the observations collected by Stetson et al. (2019). For the B band, the agreement within 1% is limited to the range $0.2 \lesssim G_{BP} - G_{RP} \lesssim 2.4$, with sizable trends outside, and typical $\sigma \simeq 0.04 - 0.05$ mag, to be attributed to poorer performances in both the photometries in this passband. As we show below, part of the observed scatter may be due to field-to-field inhomogeneities in the the Stetson's sample.

Figure E.2 focuses on the comparison in the U band. The grey dots shows the entire sample, while those plotted with the viridis density scale have `flux_U/flux_error_U>30`. If we limit ourselves to this high-S/N sample and consider the median ΔU, we conclude that the two independent sets of JKC U magnitudes agree within ≃ 3.0% over the range $-0.4 \leq G_{BP} - G_{RP} \leq 1.0$. For redder colours, the onset of a colour trend is perceivable, reaching $\Delta U \leq -0.05$ mag for $G_{BP} - G_{RP} \geq 1.3$. The typical scatter is $\sigma \simeq 0.09$, but the distribution of grey points illustrates very clearly how the performances may worsen for S/Ns lower than 30, especially at red colours (here $G_{BP} - G_{RP} \gtrsim 0.8$). We feel that this plot serves as a further invitation to exercise caution in the use of UV XPSP, even when limited to the set included in the GSPC.

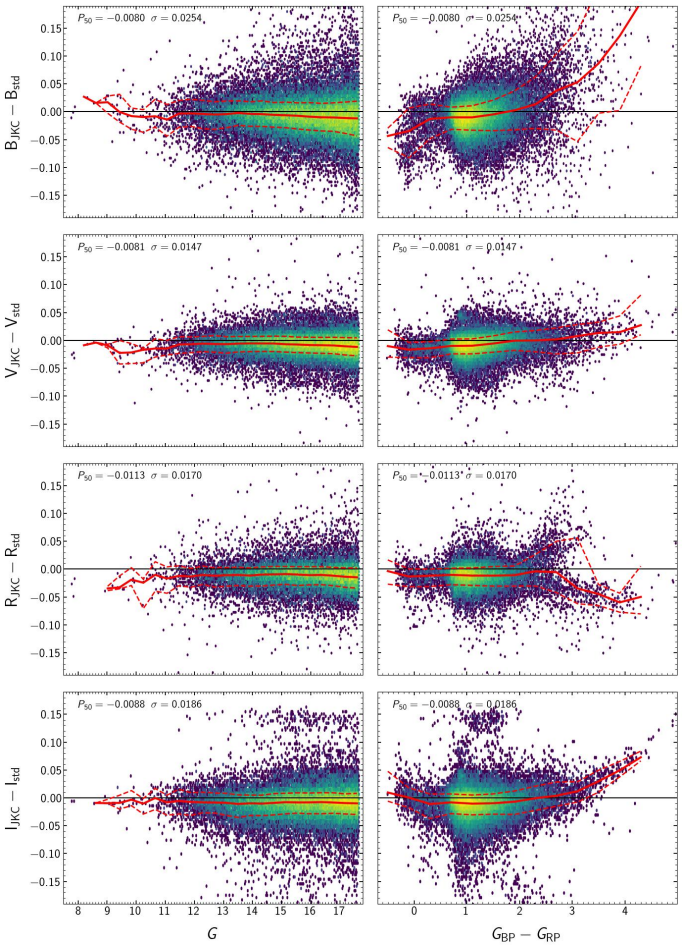

Fig. E.1. Performances of standardised XPSP in the JKC system (*BVRI*) for the Stetson validating sample. We show Δmag as a function of G magnitude (left panels) and $G_{BP} - G_{RP}$ colour (right panels) for the subsample of reference stars whose XP spectra has been released in *Gaia* DR3 and $G < 17.65$ (50468 stars). The arrangement and the meaning of the symbols is the same as in Fig. 6.

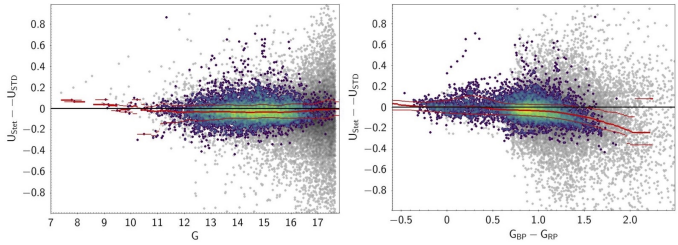

Fig. E.2. Performances of standardised XPSP in the U band of JKC system for the Stetson validating sample. The meaning of the symbols and the arrangement of the plot are the same as in Fig. E.1, except for the *y*-axes scale, which is much more expanded here. The 29176 stars in the Stetson validating sample having their XP spectra released in *Gaia* DR3, $G < 17.65$, and valid U_{Stet} and U_{STD} magnitudes are represented as grey dots, while those shown as a viridis density maps are the 9157 that also have `flux_U/flux_error_U>30`. P_{50}, P_{16}, and P_{84} lines refer to the latter subsample.

Appendix F: Examples of queries

Thanks to the availability of the GSPC table (`gaiadr3.synthetic_photometry_gspc`) along-side other *Gaia* DR3 tables, it is straightforward to perform various selections and extraction of additional parameters from the archive interface. In this Appendix we provide an example. Users will be able to modify the example query to fulfill their needs.

The query

```
SELECT dr3.source_id, dr3.ra, dr3.dec, dr3.
    parallax, dr3.parallax_over_error, dr3.ruwe,
    gspc.g_sdss_mag, gspc.i_sdss_mag FROM gaiadr3.
    gaia_source AS dr3
INNER JOIN gaiadr3.synthetic_photometry_gspc AS
    gspc
ON dr3.source_id=gspc.source_id
WHERE ABS(gspc.c_star)<(0.0059898 + 8.817481e-12 *
     POWER(dr3.phot_g_mean_mag, 7.618399))
```

joins the GPSC table with the main `gaia_source` table and selects a few parameters from each but only for sources that have an absolute corrected BP/RP flux excess factor smaller than the 1σ relation suggested in Riello et al. (2021).

The resulting dataset can be reduced in size by using the `random_index` available in `gaia_source`: For instance, by adding

```
AND dr3.random_index<1811709
```

the query would effectively run on a 0.001 random selection of the *Gaia* source catalogue. Similar joins can of course be made with a user-defined input list of source identifier.

The result of this can then be uploaded as a new user-defined table, here called `gspc_plus`. The user could then for instance generate a CMD in SDSS $g-i$ as colour and absolute magnitude $g_{\rm abs}$ (here simply computed using the inverse of the parallax to approximate the distance). The following query shows how to do this:

```
SELECT col_index / 40 AS col, mag_abs_index / 10
    AS mag_abs, n FROM (
SELECT
   floor((g_sdss_mag-i_sdss_mag) * 40) AS
       col_index,
   floor((g_sdss_mag + 5 * log10(parallax) - 10) *
        10) AS mag_abs_index,
   count(*) AS n
FROM user_xxxx.gspc_plus
WHERE parallax_over_error > 5
GROUP BY col_index, mag_abs_index
) AS subquery
```

On the other hand, the following query extracts some parameters from `gaiadr3.gaia_source` and some from `gaiadr3.synthetic_photometry_gspc`, taking all the relevant GSPC quantities for the selected photometry, for a cone of radius 1.0 deg centred on the globular cluster NGC 5139 (ω Centauri):

```
SELECT dr3.source_id, dr3.ra, dr3.dec, dr3.pmra,
    dr3.pmra_error, dr3.pmdec, dr3.pmdec_error,
    dr3.ruwe,
gspc.c_star, gspc.u_jkc_mag, gspc.u_jkc_flux,
gspc.u_jkc_flux_error, gspc.u_jkc_flag,
gspc.b_jkc_mag, gspc.b_jkc_flux,
gspc.b_jkc_flux_error, gspc.b_jkc_flag,
gspc.v_jkc_mag, gspc.v_jkc_flux,
gspc.v_jkc_flux_error, gspc.v_jkc_flag,
gspc.y_ps1_mag, gspc.y_ps1_flux,
gspc.y_ps1_flux_error, gspc.y_ps1_flag,
gspc.f606w_acswfc_mag, gspc.f606w_acswfc_flux,
gspc.f606w_acswfc_flux_error, gspc.
    f606w_acswfc_flag
FROM gaiadr3.gaia_source AS dr3
JOIN gaiadr3.synthetic_photometry_gspc AS gspc
ON dr3.source_id=gspc.source_id
WHERE
CONTAINS(
       POINT('ICRS',dr3.ra,dr3.dec),
       CIRCLE(
              'ICRS',
              COORD1(EPOCH_PROP_POS
                  (201.697,-47.479472,.1368,-3.2400,
              -6.7300,234.2800,2000,2016.0)),
              COORD2(EPOCH_PROP_POS
                  (201.697,-47.479472,.1368,-3.2400,
              -6.7300,234.2800,2000,2016.0)),
              1)
)=1
```

Appendix G: Δ mag diagrams for standardised systems

In this Appendix, we show the Δmag distributions as a function of G magnitude and BP-RP colour, before and after the standardisation process –as done in Fig. 6 and Fig. 9 for the SDSS and JKC systems– for all the remaining standardised systems discussed in Sect. 2.2 and Sect. 4, including the JKC U and SDSS u bands discussed in Sect. 3.3. The reference sets of standard stars adopted are described there. In all the figures, comparisons of Δmag as a function of G magnitude are performed on the entire reference sample, including $G > 17.65$ stars that are required to model the hockey-stick effect, while those of Δmag as a function of G_{BP}-G_{RP} colour are limited to the subsample of stars with XP spectra released in DR3 (see Sect. 2).

The Δmag distributions for the standardised UV magnitudes are presented in Fig. G.1 and Fig. G.2. Those for the PS1 system are shown in Fig. G.3, with a focus on variable stars and high $|C_\star|$ stars in Fig. G.4. The cases of the standardised HUGS and Strömgren magnitudes are illustrated in Fig. G.5 and Fig. G.6, respectively.

The values of P_{50}, P_{16}, and P_{84} as a function of G magnitude for the Δmag distributions of stars of the reference samples with XP spectra released in DR3, for the PS1, HUGS, and Strömgren standardised magnitudes are listed in Tables G.1, G.2, and G.3, respectively, in the same way as done for the SDSS and JKC systems in Tables 1 and 2, respectively.

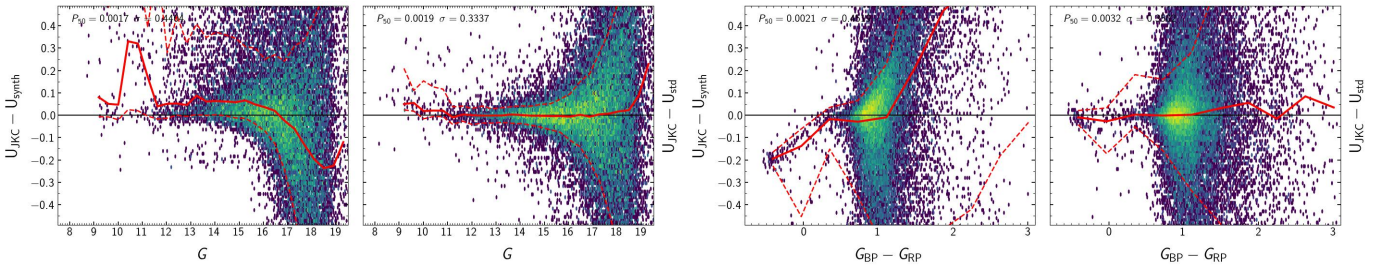

Fig. G.1. Performance and standardisation of JKC U band XP synthetic magnitudes using the reference sample described in Sect. 3.2. Left set of panels: Δmag as a function of G magnitude for the entire sample using nominal XP synthetic magnitudes (left panel) and standardised XP synthetic magnitudes (right panel). In each panel, the continuous red line connects the median Δmag computed in 0.2 mag wide bins, the dashed red lines connect the loci of the 15.87% (P_{16}) and the 84.13% (P_{84}) percentile computed in the same bins. The median (P_{50}) and the difference between P_{84} and P_{16}, here used as a proxy for the standard deviation σ, for the entire sample are reported in the upper left panel of each panel. Right set of panels: the same for Δmag as a function of BP-RP colour, limited to the subsample of reference stars having XP spectra released in DR3.

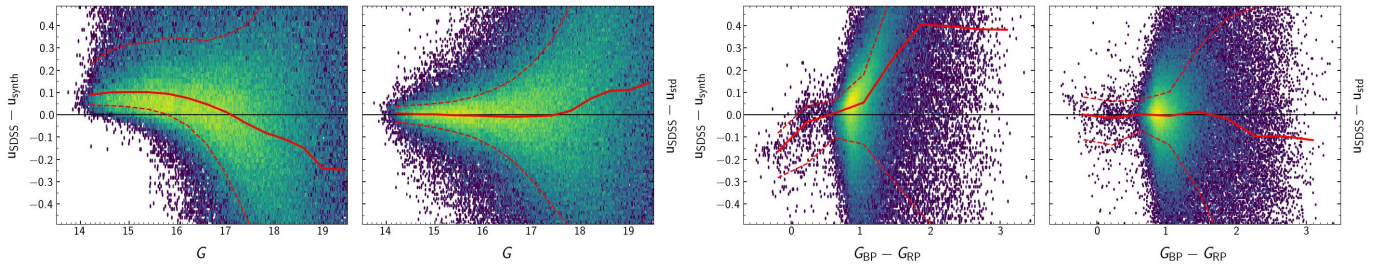

Fig. G.2. Performance and standardisation of SDSS u band XP synthetic magnitudes using the reference sample described in Sect. 3.1. The arrangement of the plots and symbols are the same as Fig. G.1, above.

Table G.1. PS1 system: median ($P_{50)}$) and 15.87% (P_{16}) and 84.13% (P_{84}) percentiles of the Δmag distributions of Fig. 13. $n_\star$ is the number of sources in the considered bin.

G mag	$P_{50}(\Delta g)$ mmag	P_{16} mmag	P_{84} mmag	$P_{50}(\Delta r)$ mmag	P_{16} mmag	P_{84} mmag	$P_{50}(\Delta i)$ mmag	P_{16} mmag	P_{84} mmag	$P_{50}(\Delta z)$ mmag	P_{16} mmag	P_{84} mmag	$P_{50}(\Delta y)$ mmag	P_{16} mmag	P_{84} mmag	$n_\star$
14.0	8.7	1.2	14.9	6.5	-0.1	12.0	2.7	-2.3	13.3	4.8	-3.2	9.9	-4.2	-10.8	2.4	40
14.4	6.6	-0.6	13.4	8.2	-0.0	16.1	3.8	-1.7	11.4	5.0	-2.5	12.7	-3.6	-11.8	7.1	138
14.8	2.6	-4.0	11.4	5.3	-1.0	12.8	4.1	-1.3	9.8	5.2	-1.3	13.2	-3.9	-14.5	6.6	308
15.2	1.7	-7.9	10.2	4.1	-4.1	11.8	3.3	-2.4	9.7	4.1	-2.6	11.5	-3.0	-14.7	7.6	584
15.6	-0.4	-10.1	8.4	2.2	-5.2	9.3	2.2	-4.4	8.1	3.5	-3.9	10.7	-2.2	-14.5	10.2	901
16.0	-0.7	-10.8	8.9	0.7	-6.8	8.5	0.8	-5.8	7.2	1.7	-5.5	9.6	-1.8	-14.9	13.4	1391
16.5	-1.9	-13.5	9.5	-1.2	-9.6	6.9	-0.7	-8.3	6.0	0.2	-8.1	8.2	-1.0	-16.4	14.9	2099
16.9	-2.2	-15.5	11.5	-2.9	-12.3	6.3	-2.4	-10.7	5.6	-1.0	-10.5	8.5	0.3	-17.6	20.4	3178
17.3	0.2	-16.0	18.3	-3.2	-14.6	7.2	-3.7	-12.9	5.2	-1.4	-11.8	9.1	2.9	-19.7	28.1	4509
17.7	2.6	-16.6	24.0	-2.9	-15.8	8.8	-3.9	-14.3	6.6	-2.2	-14.3	10.1	6.5	-21.1	35.8	2219

Table G.2. Standardised HST magnitudes: median ($P_{50)}$), 15.87% (P_{16}) and 84.13% (P_{84}) percentiles of the Δmag distributions of Fig. 14. $n_\star$ is the number of sources in the considered bin. F438W is from the WFC3/UVIS passbands set, F606W and F814W from the ACS/WFC set.

G mag	$P_{50}(\Delta F438W)$ mmag	P_{16} mmag	P_{84} mmag	$P_{50}(\Delta F606W)$ mmag	P_{16} mmag	P_{84} mmag	$P_{50}(\Delta F814W)$ mmag	P_{16} mmag	P_{84} mmag	$n_\star$
11.4	18.2	-23.4	53.8	4.6	-2.6	91.1	10.0	-6.1	84.0	36
12.2	10.6	-22.2	50.8	4.7	-9.6	25.7	-1.0	-19.3	24.0	87
13.0	3.4	-17.3	36.3	0.4	-8.1	11.3	-3.5	-14.9	12.2	117
13.8	2.6	-18.9	30.9	-1.0	-9.4	8.6	-6.8	-16.0	6.9	142
14.5	2.6	-14.2	23.9	1.7	-7.8	11.1	-2.5	-19.0	12.6	118
15.3	-4.3	-20.6	14.6	1.4	-10.4	12.9	0.8	-16.5	14.3	132
16.1	-9.3	-28.6	6.8	-2.2	-13.8	11.0	-4.1	-20.0	13.1	109
16.9	-15.4	-36.8	13.1	-7.3	-15.6	4.7	-4.1	-27.1	11.7	145
17.7	-21.4	-43.9	14.1	-7.7	-23.8	3.5	-11.2	-39.5	12.1	67